UNIVERSITYOF BIRMINGHAM

Laser Interference Lithography for the Nanofabrication of Stimuli-Responsive Bragg Stacks

Jiang, Nan; Butt, Haider; Montelongo, Yunuen; Liu, Feng; Afewerki, Samson; Ying, Guo Liang; Dai, Qing; Yun, Seok Hyun; Yetisen, Ali K.

Document Version
Peer reviewed version

[Link to publication on Research at Birmingham portal](#)

Laser Interference Lithography for the Nanofabrication of Stimuli-Responsive Bragg Stacks

Nan Jiang, Haider Butt, Yunuen Montelongo, Feng Liu, Samson Afewerki, Guo-Liang Ying, Qing Dai, Seok-Hyun Yun, and Ali K. Yetisen*

Dr. N. Jiang, Dr. S. Afewerki, Dr. G. L. Ying
Biomaterials Innovation Research Center, Engineering in Medicine Division, Brigham and Women's Hospital, Harvard Medical School, Cambridge, Massachusetts, 02139, USA
Dr. N. Jiang, Dr. S. Afewerki, Dr. G. L. Ying, Prof. S. H. Yun, Dr. A. K. Yetisen
Harvard-MIT Division of Health Sciences and Technology, Massachusetts Institute of Technology, Cambridge, Massachusetts 02139, USA
Dr. N. Jiang
State Key Laboratory of Advanced Technology for Materials Synthesis and Processing, Wuhan University of Technology, 122 Luoshi Road, Wuhan 430070, China
Dr. H. Butt
Nanotechnology Laboratory, School of Engineering, University of Birmingham, Birmingham B15 2TT, UK
Dr. Y. Montelongo
Department of Chemistry, Imperial College London, South Kensington Campus, London SW7 2AZ, UK
Prof. F. Liu
Department of Physics, Shanghai Normal University, Shanghai 200234, China
Dr. G.L. Ying
School of Materials Science and Engineering, Wuhan Institute of Technology, Wuhan 430205, China
Prof. Q. Dai
National Center for Nanoscience and Technology, Beijing 100190, China
Prof. S. H. Yun, Dr. A. K. Yetisen
Harvard Medical School and Wellman Center for Photomedicine, Massachusetts General Hospital, 65 Landsdowne Street, Cambridge, Massachusetts 02139, USA
E-mail: akyetisen@gmail.com

Abstract

Dynamic structural coloration in *Tmesisternus isabellae* beetle elytra is a unique example of Bragg stacks based wavelength tuning in response to external stimuli. The underlying dynamic coloration principles of *T. isabellae* have the potential to guide the design of quantitative optical stimuli-responsive polymers. Existing nanofabrication techniques to create such dynamic Bragg stacks are costly, time-consuming, and require high expertise. Here, we report a nanofabrication method to produce slanted Bragg stack structures in poly(acrylamide-*co*-poly(ethylene glycol) diacrylate) (p(AM-*co*-PEGDA)) hydrogel films by combining laser-directed interference lithography (LIL) and silver halide chemistry in a cost-effective and rapid process (~10 min). The Bragg stacks consisted of silver bromide (AgBr) nanocrystal (NC) multilayers having a lattice spacing of ~200 nm. Upon broadband light illumination, the Bragg stacks diffracted a narrow-band peak at 520 nm at ~10° with respect to the normal incidence. The lattice spacing of the hydrogel films can be modulated by external stimuli to shift the Bragg peak for quantitative measurements. To demonstrate the utility of this method, the Bragg stacks were functionalized with phenylboronic acid (PBA) molecules. Spectral analysis of the Bragg peak shifts allowed reversible glucose sensing within a physiological dynamic range (0.0-20.0 mmol L^{-1}) having a sensitivity of 0.2 mmol L^{-1}.

1. Introduction

Since Robert Hooke and Isaac Newton's early observations of structural color in peacock tail feathers and mother of pearl in the 17-18th centuries, electron microscopy investigations have revealed the existence of diverse nanophotonic structures in nature from 1D to 3D photonic crystals.[1] Dynamic structural coloration is rare in nature and its evolutionary functions include Batesian mimicry, camouflage, conspecific recognition, predation, signal communication, and mating behavior.[2] It involves the diffraction of an incoming broadband light (sunlight) from a hierarchy of nanostructures, in which the periodicity can be modulated

2

within the spectrum, ranging from ultraviolet light to near-infrared region.[2a] For example, the reflective stripes of the paradise whiptail (*Pentapodus paradiseus*) contain physiologically active iridophores.[3] Using the periodically stacked structure in its stripe, it can tune the color of the stripe from ultraviolet to blue to achieve interspecies recognition and communication. The Hercules beetle (*Dynastes Hercules L*). contains a yellow sponge layer with periodic pillars which display black color.[4] The color of the beetle can reversibly change from black to greenish yellow in a reversible manner when subjected to changes in humidity for thermoregulation and camouflage. The golden tortoise beetle (*Charidotella sexpunctata*) shows color changes in its cuticle from yellow to red by switching its chirped multilayer reflector to a translucent slab exposing pigmentary red substrate underneath to mimic unpalatable ladybird.[2b] Chameleons (*Furcifer pardalis*) adapt to their surroundings by displaying rapid structural color changes through active modulation of guanine NC spacing in dermal iridophores for camouflage purposes.[5]

A simple arrangement to create dynamic coloration in nature is through anatomic modulation of 1D photonic crystals (Bragg stacks), where a multilayer grating produces light interference under broadband illumination.[6] A striking example of dynamic structural coloration with Bragg Stacks is observed in *Tmesisternus isabellae* (longhorn beetles), which exhibits color changes in its elytra in response to humidity.[7] The function of this evolutionary adaptation is unknown. **Figure 1** shows color changes of the beetle elytra in response to low (40%), interim (60%) to high (80%) relative humidity. The elytra showed bright golden-yellow iridescent color under broadband light in 40% relative humidity, while the color changed from orange-red to red when the relative humidity was increased to 80% (Figure 1a). Optical microscopy investigations of the beetle elytra showed that the dynamic coloration originated from the long scales on the elytra surface at different relative humidity conditions (40-60%) (Figure 1b, Movie S1). Specifically, the structural coloration of the beetle elytra was synthesized from the multilayer interference in Bragg stacks, which could be

tuned by physiological or external stimuli.[8] Figure 1c-e and S1 show the Scanning Electron Microscopy (SEM) and Transmission Electron Microscopy (TEM) images of the multilayer structure of elytra. The elytra were composed of alternating layers of melanoprotein (~110±20 nm in thickness) consisting of densely-packed nanoparticles and air gaps (~65±15 nm) (Figure 1f, S2). The beetle elytra were bleached by hydrogen peroxide to reveal the presence of melanin (Figure S3).[9] Angle-resolved measurements also revealed that the Bragg peak shifted from 600 nm to 530 nm as the diffraction collection angle was increased from 0° to 30°with respect to normal incidence (Figure 1g). When the relative humidity (40%) was increased to 80%, water infiltration and subsequent swelling of the multilayers shifted (33 nm) the diffracted peak to longer wavelengths (Figure 1h). The decrease in the diffraction efficiency by ~44% was owing to the decreased effective refractive index (RI) of the multilayers.[7a] Water absorption by the melanoprotein layer swelled the multilayer structure and shifted the diffraction peak (λ_{max}), obeying Bragg-Snell's law (Equation 1):[6, 10]

$$\lambda_{\mathrm{max}} = 2(n_{\mathrm{m}}d_{\mathrm{m}}\cos\theta_{\mathrm{m}} + n_{\mathrm{a}}d_{\mathrm{a}}\cos\theta_{\mathrm{a}}) \tag{1}$$

where n_{m} (~2.0) and n_a (~1.2) represent the RIs of melanoprotein layer and air gap layer, d_{m} and d_{a} are the thicknesses of melanoprotein layer and the air gap layer, and θ_m and θ_a are the refraction angles with respect to normal incidence. The maximum theoretical diffraction efficiency that can be obtained from the beetle elytra was calculated to be 75% in the visible spectrum.[11] This high diffraction efficiency can be attributed to both high RI of the melanoprotein layers and the low RI of the air gap layers, providing ideal conditions for light interference and diffraction. However, the infiltration of water into the elytra fills the air gaps and swells the melanoprotein layer. As a consequence, water infiltration decreases the RI of the Bragg stack, decreasing the diffraction efficiency by more than 40%. Additionally, the hierarchical distribution of the elytra over the dorsal side of the beetle ensures that the diffraction can be observed from large viewing angles. The beetle elytra have shown the ability to sense humidity changes by diffracted color changes. Hence, these physical

principles of dynamic structural coloration can be used as a guideline to create tunable optical nanostructures to quantitatively sense analyte changes.[12]

Based on the understanding of the exquisite hierarchical dynamic structures in nature, several bottom-up and top-down nanofabrication approaches have been developed to create stimuli-responsive nanophotonic structures.[13] Bottom-up nanofabrication approaches include layer-by-layer deposition, self-assembly of diblock copolymers, and spincoating.[11a, 14] These approaches have challenges due to time-consuming layer deposition, inability to functionalize layers, and uneven layer thicknesses, as well as high-cost laborious production of Bragg stacks.[15] As a top-down nanofabrication approach, laser interference lithography (LIL) has emerged as a rapid and flexible technique to produce multilayer gratings.[16] LIL is a maskless technique that creates Bragg stacks by using two or more coherent laser waves.[17] The commonly used pulsed laser (nanosecond or femtosecond) provides a high peak power that allows the formation of Bragg stacks by laser ablation.[18] In addition to the high cost of nanosecond pulsed laser ($1-50k),[18a, 19] laser ablation based production of Bragg stacks is affected by nanoparticle light scattering, particle attenuation, and damage to the recording medium, limiting the diffraction efficiency of the resulting photonic nanostructure. The multiphoton absorption polymerization can also be utilized to fabricate Bragg stacks; however, they are limited as active radicals that polymerize monomers in the antinodes diffuse into the dark fringe regions, which results in relatively low resolution.[20]

Continuous wave (CW) laser light interference combined with silver halide chemistry provides a cost-effective method to create controllable Bragg stacks with high diffraction efficiency. However, the fabrication of Bragg stacks by CW laser interference typically requires complex laser optics and setups.[21] The need for high-cost pulsed or continuous wave (CW) laser setups and optical equipment complexity have limited the adoption of LIL in photonic nanostructure production.[22] Additionally, due to the complexity of optical laser writing setups involving the alignment of multiple mirrors and beam expanders, the systems

requires stabilization to reduce environmental vibrations. Hence, there is a clear need to develop a cost-effective nanofabrication method that allows Bragg stacks to be fabricated rapidly and reproducibly Bragg stacks without the need for complex laser optics.

In this work, we created a cost-effective LIL nanofabrication method for the rapid production of Bragg stacks embedded in hydrogel films. A low-cost portable laser diode was utilized to create a periodic interference pattern within the photosensitized p(AM-*co*-PEGDA) hydrogel film in Denisyuk reflection mode. A latent image was recorded using silver halide chemistry to form periodic AgBr NC multilayers in the hydrogel film. To demonstrate the utility of the stimuli-responsive Bragg stacks, the p(AM-*co*-PEGDA) hydrogel backbone was functionalized with 3-(acrylamido)phenylboronic acid (3-APBA) to produce a reversible response to variation in glucose concentration, which was correlated with Bragg peak shifts to obtain quantitative measurements.

2. Results and Discussion

To rationally design a Bragg stack that can dynamically operate in the visible spectrum, a finite element method was utilized to model and study a multilayer structure. In a dynamically tunable system, it is expected that as the lattice spacing increases, the Bragg peak will shift to longer wavelengths (**Figure 2**a). To build the Bragg stacks, AgBr NCs were chosen due to its light-sensitivity and high RI (2.28, λ=546 nm). The designed domain was modeled to simulate a polymer film (thickness ~10 μm, RI= ~1.46) with alternating multilayer AgBr NC stacks. These Bragg stacks filter incoming broadband light and diffract narrow-band rays in the visible spectrum. Figure 2b shows the finite element simulations of Bragg stacks having lattice spacings ranging from 150 nm to 180 nm. The wave propagation simulations for a lattice spacing of 150 nm showed a Bragg peak position of 520 nm. This wavelength defines the green diffracted color of the Bragg stacks, where the Bragg peak position is primarily dictated by the lattice spacing between the AgBr NC stacks. The effect of lattice spacing expansion on the position and intensity of the Bragg peak was also analyzed. As the number

of the Bragg stacks and AgBr NCs were kept constant (40 NCs per stack), the Bragg stack geometry was laterally expanded. The lateral expansion increased the lattice spacing of the Bragg stacks and reduced the concentration of AgBr NCs within a stack. As the lattice spacing increased from 150 nm to 180 nm, the diffracted spectra produced a red-shift, changing the color from green to orange (Figure 2c). The diffraction efficiency of the Bragg stack peak decreased by 15%, while the lattice spacing increased by 30 nm. This phenomenon could be ascribed to the decreased concentration of AgBr NCs within a stack reducing the RI-contrast between the stacks and the surrounding medium. According to the Bragg's law, the diffraction spectrum could be correlated to the effective RI of the stacks and their lattice spacing. The factors that influence the diffraction ray could be described as (Equation 2):[11a]

$$\frac{\Delta\lambda}{\lambda} = \frac{\Delta n}{n} + \frac{\Delta d}{d} + \cot\theta\,\Delta\theta \tag{2}$$

where $\Delta\lambda$, Δn, Δd, $\Delta\theta$ are changes in Bragg peak wavelength, effective RI, lattice spacing, and diffraction angle. To analyze the outcome of effective RI changes (Δn) within the Bragg stacks, the concentration of AgBr NCs was varied within a Bragg stack, where d (150 nm) and θ (90° from the normal incidence) were kept constant (Figure 2d). As the effective RI of the AgBr NC stack was increased from 1.49 to 1.70 (corresponding to 20 to 80 AgBr NCs per stack), the diffraction efficiency increased by 83% (Figure 2e). This indicated that increasing AgBr NCs density enhanced the diffraction efficiency. Additionally, the increase in the effective RI of the stack by 0.21 resulted in the Bragg peak shift by ~30 nm to longer wavelengths.

The Bragg stack embedded in a 10 µm thick p(AM-*co*-PEGDA) hydrogel film was fabricated by free-radical polymerization on a silanized glass surface (Table S1, Scheme S1). The Bragg stacks within the hydrogel matrix were formed by a cost-effective and rapid LIL method involving silver halide chemistry (**Figure 3**a, Table S2). Ag+ ions were diffused into the synthesized hydrogel film (Figure 3a-i). Photosensitization was achieved by exposing the hydrogel film to a solution containing LiBr and acridine orange dye, which converted the Ag+

ions to photosensitive AgBr NCs (Figure 3a-ii, 3b-i). An optical interference setup was configured to operate in Denisyuk reflection mode for writing a latent image within the hydrogel matrix using a CW laser diode (λ=532 nm, 5 mW) (Figure 3a-iii, 3b-ii).[23] Ascorbate buffer was diffused into the hydrogel film, which was sandwiched using another glass substrate. The photosensitive film was placed on a leveled surface tilted (5°) from the surface plane of a plane mirror. Figure 3c shows the optical setup for writing a latent image in the AgBr NCs using the portable laser diode. The inset in Figure 3c shows the mechanism of the laser light interference of an incident beam (reference wave) and a reflected beam from the plane mirror (object wave). The constructive interference (antinodes) corresponded to high laser intensity regions of a standing wave. This process created a multilayer latent image within the hydrogel film.

Upon the formation of an interference pattern, photosensitive dye on the surface of AgBr NCs absorbed photons. The process underwent proton-coupled electron transfer, in which electrons transferred from a ground state to an excited state, subsequently releasing electrons ($AgBr + h\nu \rightarrow Ag^+ + Br^0 + e^-$) (Figure 3d).[24] The interstitial Ag^+ ion left its original position to an "interlattice" space due to thermal equilibrium (Figure 3e-i, Equation S1). The released electrons migrated to an electron trap zone in the latent image site, offering a negatively charged trap zone (Figure 3e-ii). The intensity of the laser exposure light determined the amount of photon-electron transfer in the photosensitive dye. However, the ascorbate buffer (pH 6.0) also acted as the electron source for photo-induced electron transfer (Scheme S2). In electron conduction stage, the negatively charged site attracted positively-charged interstitial Ag^+ ions that were deposited in the latent image site (Figure 3e-iii). When the interstitial Ag^+ ions reached to the trap site, the positive charge was neutralized ($Ag^+ + e^- \rightarrow Ag^0$). The Ag speck was formed by accumulating Ag atoms on the latent image site (Figure 3e-iv). The latent image was amplified using a photographic developer. The reduction of AgBr NCs to Ag^0 NPs is normally carried out using a highly alkaline developer (pH >12).[25] However,

alkaline developers distort the polymer chains and results in hydrolyzation.[26] In the present work, a neutral developer was used to convert Ag atoms in the AgBr NCs to Ag^0 NPs (Figure 3a-iv). The neutral developer provided electrons that allowed Ag^+ ions in the "interlattice" position to adhere to the latent image Ag atoms (Scheme S3). Therefore, the Ag^0 NPs grew until the developer was neutralized by decreasing the pH using acetic acid (Figure 3a-v). The excess AgBr grains and conjugated photosensitive dye were removed from the hydrogel matrix by rinsing with a hypo solution containing sodium thiosulphate (Figure 3a-vi, 3b-iii). The unreacted Ag^+ ions and AgBr NCs binded to the terminal sulfur in thiosulphate to form soluble compounds (Scheme S4).

Ag^0 NPs can be used as diffractive layers in Bragg stacks; however, the RI of Ag^0 NPs ($n=0.14+i\,3.14$, $\lambda=546$ nm) results in low diffraction efficiency.[27] Low diffraction efficiency makes the diffracted peak of Bragg stacks difficult to be observed or detected, which affects the performance of the sensor including sensitivity, response and reset time and detection limits. To increase the diffraction efficiency of the Bragg stacks, Ag^0 NPs were converted back to AgBr NCs by copper sulfate oxidation in a bleaching bath containing Br^- ions (Figure 3a-vii, Scheme S5). The reduced Cu^0 NPs in the hydrogel film were removed by an anti-printout solution containing persulfate and hydrogen sulfate ions (Figure 3a-viii, 3b-iv, Scheme S6). Meanwhile, free bromide produced from the solution attached to the AgBr NCs surface and acted as a strong oxidant to protect the AgBr NCs from converting back to Ag^0 NPs by photolysis. Movie S2 shows a simulation of the entire LIL process to produce the Bragg stacks. The whole fabrication process was performed in less than 10 min.

The process of latent image formation in LIL has been studied to understand the optical properties of the Bragg stacks. To simulate LIL patterning process, the exposure radiant fluence and fabrication speed were defined as ~50 mJ cm^{-2} and 0.5 cm^2 s^{-1}, respectively. The fabricated hydrogel film was measured to be ~10 μm thick (Figure S4). **Figure 4**a shows the field distribution within a 10 μm thick recording medium with a tilt angle of 5°, where the

absorption was assumed to be 18%. The incidence laser beam (λ=532 nm) was propagated through the boundary in Denisyuk reflection mode. The localization of light intensity had an essential role in the standing wave formation. The decreases in the exposure radiant fluence was 18% over a ~10 μm propagation distance (Figure 4b). The localized standing wave intensity had a lattice spacing of ~200 nm (Figure 4b inset, S5). Along with the vertical periodicity to form a multilayer exposure pattern, a lateral interference pattern having a periodicity of ~1.5 μm was also observed and this could be attributed to the internal reflections.

The diffraction spectra of Bragg stacks were collected using a spectrophotometer with the illumination of incident broadband light (Figure S6). The Bragg stacks containing AgBr NCs diffracted green color with diffraction efficiencies of 9% (Figure 4c, d). Moreover, the Bragg stacks in the form of hydrogel films were shaped to various geometries such as free-standing round flakes (Ø= 2.0 mm). The hydrogel flakes maintained green diffraction color under broadband light (Figure 4c inset). The spectrum of the Bragg stacks containing AgBr NCs had a central peak at ~520 nm and diffracted light at ~10° from the normal interference and the full width at half-maximum was 13.4 nm (Figure 4d). The fabricated Ag^0 NP Bragg stack was shown in Figure S4b and the size of the Ag^0 NPs was ~10 nm (Figure 4d inset). To understand the parameters that affect the diffraction efficiency, the Ag^+ ion concentrations in the hydrogel films were analyzed. As the Ag^+ ion concentration in the hydrogel film increased from 1.0 to 100.0 mmol L^{-1}, the density of the formed Ag^0 NPs increased from 0.08% to 0.20% and it saturated at a Ag^+ ion concentration of ~80 mmol L^{-1} (Figure 4e). The diffraction efficiency of the AgBr NC stack increased from 4.2% to 8.5% as the Ag^+ ion concentration increased from 25 to 100 mmol L^{-1} (Figure 4f). The diffraction efficiency of Bragg stack was saturated at Ag^+ ion concentration of 100 mmol L^{-1}, which was consistent with the saturation point of Ag^0 NPs density within the hydrogel film.

To demonstrate the utility of the Bragg stacks, a phenylboronic acid derivative was incorporated to render the hydrogel matrix sensitive to glucose.[28] Phenylboronic acid derivatives have been known to covalently bind with *cis*-diol groups of carbohydrates to form boronic esters.[29] Figure S7 shows the reversible complexation equilibrium of phenylboronic acid with *cis*-diol groups of glucose molecules.[30] At low pH value, the phenylboronic acid is in trigonal planar form (unchanged state), which does not complex with glucose. However, above its pKa value (> 8.8), the phenylboronic acid is in tetrahedral state (negatively charged state), which can readily bind with *cis*-diol groups of glucose.[31] When the phenylboronic acids are incorporated within a hydrogel matrix, they can be used as reversible and real-time glucose-responsive hydrogel films. In the presence of a high ionic strength buffer (150 mmol L^{-1}), the hydrogel was fully swollen prior to experiments. Hence, the complexion of phenylboronic acid and the *cis*-diol groups of glucose molecules in subsequent hydrogel expansion could be explained by the modified Flory-Huggins theory (Equation S2-S6).[32] p(AM-*co*-PEGDA-*co*-3-APBA) hydrogel flakes responding to glucose were investigated and p(AM-*co*-PEGDA) hydrogel flakes were used as a control. The optimization in PEGDA and 3-APBA showed that the precursor of the hydrogel with AM (77 mol%), PEDGA (3 mol%), and 3-APBA (20 mol%) had the largest expansion (2.9%) in response to glucose (10 mmol L^{-1}, 24 °C) which was optimal for glucose response. The complexation of 3-APBA and glucose reached to the saturation points after 40 min. When glucose molecules diffused into the p(AM-*co*-PEGDA-*co*-3-APBA) hydrogel films, glucose-boronic acid complexation decreased the pK_a of the PBA groups upon *cis*-diol binding, resulting in charged boronate groups. The formation of anionic boronate increased the Donnan osmotic pressure of the system, resulting in hydrogel swelling. The hydrogel expansion curves were fitted to Equation 3 which describes the hydrogel diameter expansion ($\Delta\emptyset(t)$) correlated with glucose diffusion dynamics:

$$\Delta\emptyset(t) = \Delta\emptyset_{\infty}\sqrt{1 - e^{-\alpha t}} \tag{3}$$

where $\Delta\emptyset_\infty$ is the hydrogel flake diameter expansion after an infinite time, α represents the decay constant, and t is the diffusion time. When using higher concentrations of PEGDA as the crosslinker (4.0 and 3.5 mol%), the elasticity of the hydrogel flake decreased, resulting in hydrogel diameter expansions of 1.7% and 2.5%, respectively. However, the hydrogel flakes with low concentration of PEGDA did not show significant swelling (2.2% and 1.1% diameter expansion) (**Figure 5**a). With increasing 3-APBA concentration (25, 30 mol%) at a constant PEGDA concentration (3 mol%), hydrogel diameter expansion was limited to 1.7% and 1.1%, respectively. This could be attributed to the decreased in AM concentration. Another factor that affected hydrogel expansion was the low solubility of 3-APBA in DI water. At low concentrations of 3-APBA (10-15 mol%), the hydrogel swelling was low (1.1% and 2.6 mol%) due to low complexion of phenylboronic acid and *cis*-diol groups of glucose molecules (Figure 5b). The effect of the pH value on hydrogel flakes expansion depended on the apparent pK_a value. Hydrogel flakes expanded 5.9% by increasing the pH value of the buffer solution (150 mmol L^{-1}) from 4.5 to 9.0 (Figure 5c and S8, Table S3). Apparent pKa value of the hydrogel flake was calculated from the modified Henderson-Hasselbalch equation which could be expressed as (Equation 4):

$$\emptyset_{\text{shift}} = \Delta\emptyset \, (1 + 10^{(pKa-pH)})^{-1} \qquad (4)$$

where $\emptyset_{\text{shift}}$ is the hydrogel flake diameter change, $\Delta\emptyset$ represents the difference between maximum and minimum of flake diameter, pKa represents the acid dissociation constant. Based on Equation 4, the apparent pKa value was ~7.8. As the glucose concentration increased within the physiological range from 5 mmol L^{-1} to 20 mmol L^{-1}, the p(AM-*co*-PEGDA-*co*-3-APBA) hydrogel flake diameter expansion increased from 1.4% to 7.7% within 40 min. Without 3-APBA molecules, hydrogel flakes did not show significant expansion (Figure 5d and S9, Table S4). The effect of ionic strength on hydrogel shrinkage was also investigated by immersing hydrogel flakes in metal ion solutions (Na$^+$, K$^+$, Ca^{2+} and Mg^{2+} ions, pH=7.4). As ion concentrations increased from 5 mmol L^{-1} to 200 mmol L^{-1}, the

diameter of hydrogel flakes shrunk 0.8%, 0.8%, 0.9% and 1.4%, respectively (Figure 5e and S10, Table S5). The fully-swollen hydrogel flake shrinkage could be attributed to the increase in counterions that amplified the Donnan osmotic pressure.[33] The interference in hydrogel expansion might be caused by physiological fructose and lactate commonly found analytes in biological samples, which could also bind to 3-APBA. Due the its smaller molecular weight (Mw=90 g mol^{-1}), lactate rapidly diffused into the hydrogel matrix and bound to boronic acid groups, achieving fast equilibrium within 20 min. Replacing the glucose solution with fructose solution (pH=7.4) resulted in a higher hydrogel flake expansion (3.1%) within 30 min as compared to glucose (2.7%) (Figure 5f and S11, Table S6). These results were consistent with the previous studies that showed that boronic acid had higher affinity to fructose than glucose.[34]

After the optimization of the phenylboronic acid formulation, a Bragg stack was incorporated into a hydrogel film to create an analytical device to quantitatively report the concentration of glucose. The phenylboronic acid-*cis* diol complexation and subsequent hydrogel swelling increased the lattice spacing of periodically distributed AgBr NC stacks, shifting the Bragg peak to longer wavelengths (**Figure 6**a). The concentration of glucose can be correlated with the wavelength of the Bragg peak. In the presence of a glucose solution (100 mmol L^{-1}) in buffer (pH 7.4, 150 mmol L^{-1}) at 24 °C, the peak of Bragg stack shifted from its original position at 520 nm to 576 nm in 90 min (Figure 6b). Bragg stacks synthesized without 3-APBA co-monomers shifted the diffraction peak by 1-2 nm, indicating its crucial role in glucose complexation (Figure 6b inset). The minimum resolution of the Bragg peak that could be measured using a spectrophotometry was 0.50 nm, which correlated to a minimal lattice spacing swelling of 0.17 nm. Theoretically, the Bragg stack hydrogel film (~10 μm in thickness) needs to swell to a minimum of 8.8 nm to produce a resolvable wavelength shift in the spectrum.

The diffraction efficiency of the Bragg stacks asymptotically decreased by ~65% during the hydrogel film expansion, which could be owing to the decreased concentration of the AgBr NCs per stack. The correlation between the maximum diffraction intensity and the position of the Bragg peak was (Equation 5):

$$DE_{max} \approx DE_0 + \frac{c}{\lambda_{peak} - \lambda_0}$$ (5)

where DE_0 and λ_0 are the asymptotes of the fitting curve, and c is a constant. As the Bragg peak shifted 50 nm (from 520 nm to 570 nm), the diffraction efficiency decreased 5.4%, which was consistent with the simulated 5.5% decrease of diffraction efficiency as the Bragg peak shifted from 510 nm to 560 nm (Figure 2c). The Bragg peak shift was associated with visible color changes from green to orange to orange-red (Figure 6b inset). The complexation of the anionic boronate with *cis*-diol groups of glucose molecules showed an exponential decay over time. The characteristics of the Bragg stacks response was modeled by analyzing the dynamic Bragg peak shift behavior in response to glucose. During complexation, the concentration of the bound glucose molecules can be expressed as (Equation 6):

$$C_i(t) = C_\infty(1 - e^{-\gamma t})$$ (6)

where C_∞ is the amount of anionic boronate form at infinite time, γ is the binding rate of boronic acid-*cis* diol complexation, and t is the analyte complexation time. Within the physiological range of glucose concentration, the complexation is proportional to the Bragg peak shift:

$$\Delta\lambda(t) = \Delta\lambda_\infty(1 - e^{-\gamma t})$$ (7)

where $\Delta\lambda_\infty$ represents the equilibrated Bragg peak shift. Therefore, Equation 7 can be used to describe Bragg peak shift over time. The response of the Bragg stack to glucose concentration was tested within physiological glucose conditions (*e.g.*, diabetic range of 3-20 mmol L^{-1}, normal: 4.2-6.4 mmol L^{-1}) (Figure 6c and S12). The Bragg stack was fully swollen before the measurements. With boronate anion and glucose complexation, the Donnan osmotic pressure increased and the Bragg peak shifted by 5 and 12 nm for glucose concentrations of 5 and 20

mmol L^{-1}, respectively over 1 h. The Bragg peak shift saturated with increasing glucose concentrations (Equation 7). The average sensitivity of the Bragg stack was calculated to be 0.2 mmol L^{-1} (Figure S13 "Sensitivity of the Bragg Stacks").

The reversibility of the glucose-responsive hydrogel and the embedded Bragg stack was measured. Four consecutive hydrogel resetting experiments were performed within 70 min in a buffered glucose solution (10 mmol L^{-1}) (Figure 6d). Replacing the glucose solution with an acetate buffer (pH=4.6) resulted in hydrogel shrinkage. This process broke the covalent bonds between the phenylboronic acids and *cis*-diols of glucose. The hydrogel swelled back to its original size by replacing the acetate buffer with a glucose-free phosphate buffered saline (PBS) solution (pH=7.4), enabling reusability of the glucose-responsive hydrogel. As the glucose-free solution was replaced with a glucose solution (20 mmol L^{-1}), the diameter of the hydrogel flake expanded by 4.6%. When the glucose solution was replaced with a glucose-free solution, the hydrogel shrank by 3.4% (Figure 6e).

Subsequent experiments were performed to validate the hydrogel reversibility with a Bragg stack. When the glucose-free solution was replaced with a glucose solution (5 mmol L^{-1}), the Bragg peak shifted by 5 nm over 1 h at 24 °C (Figure 6f). The replacement of the glucose solution (pH 7.4) with acetate buffer (pH 4.6) transformed the tetrahedral state of anionic boronate to an uncharged trigonal state, releasing the glucose molecules from the hydrogel matrix within 10 s. The decrease in the lattice spacing of the Bragg stack with acetate buffer could be attributed to the decrease of pH below the apparent pK_a value of the hydrogel, shifting the Bragg peak to shorter wavelengths (λ_{peak}=510 nm). When the acetate buffer was replaced with a glucose-free buffer solution (pH 7.4), the Bragg peak shifted to its original position (λ_{peak}=520 nm) and no hysteresis was measured in resetting the Bragg stack over multiple trials (Figure 6f). As glucose-free solutions were replaced with glucose solutions at concentrations of 10, 15, and 20 mmol L^{-1}, the Bragg peak shifted 7.4, 8.9, and 12.0 nm respectively, which was consistent with the results of individual measurements of

each glucose concentration (Figure 6c). The Bragg peak shifted to shorter wavelengths (λ_{peak}=510 nm) when acetate buffer was applied for resetting. These results demonstrated that the phenylboronic acid functionalized Bragg stack could be used for the reversible glucose measurements without hysteresis.

3. Conclusion and Discussion

Dynamic structural colorations of *T. isabellae* elytra in response to the variations in environmental humidity were attributed to Bragg peak shifts from the alternating melanoprotein-air layers. To reproduce this multilayer structure and resemble its dynamic coloration properties, we created a cost-effective method to rapidly fabricate a stimuli-responsive slanted Bragg stack by combining LIL and silver halide chemistry. The produced Bragg stack could accurately report the changes of glucose concentrations by diffraction peak shifts without being affected by intensity changes. However, as compared to high diffraction efficiency in beetle elytra (~75%), the fabricated Bragg stack had low diffraction efficiency (~9%) due to the low effective refractive index contrast and low particle density within the hydrogel film. To improve the diffraction efficiency, the AgBr NCs density can be improved by utilizing more hydrophilic polymers for optimal AgNO$_3$ perfusion into the hydrogel matrix. The AgBr NCs can also be replaced by high-RI materials such as TiO$_2$ nanoparticles and synthetic photopolymers which can tune the RI by varying concentrations of polymer.[35] The melanoproteins could be used to produce Bragg stacks by a layer-by-layer deposition process.[36] However, the melanoproteins as pigments, they are easily affected from bleaching, which could render Bragg stack sensors instable. Furthermore, the Bragg stack had a narrow diffraction angle (~10°), which required a specialized spectroscopy setup to measure the diffraction peak shifts. To overcome this challenge, angular tolerance can be improved by replacing the plane mirror with a convex mirror during the LIL process to distribute the diffracted light broader angles (Figure S14).[11a] Moreover, the object used to create the latent image can be substituted with other complex structures to form a wide range of grating shapes (*e.g.*, arrays, 2/3D patterns and images).[18a]

To improve the selectivity for glucose, other PBA derivatives can be utilized, such as 2-(acrylamido)phenylboronate, *bis*-boronic acid, and 4-vinylphenylboronic acid.[31, 37] Additionally, the hydrogel matrix can be functionalized with other receptors to create

selectivity for other analytes including ions, proteins, and microorganisms.[15a, 22, 38] The sensitivity of the Bragg stack hydrogel can also be enhanced by using other highly elastic polymers which could increase the polymer swelling in response to external stimuli. Synthesizing the hydrogel matrix to produce nanoporous structures and a gating membrane can enhance analyte diffusion and complexation rate by increasing the surface area.[39] The Bragg stack hydrogels can be easily shaped to various geometries such as flakes that can be integrated with commercial test strips or implantable devices.[28, 40] A single hydrogel film on a microscopy glass slide can be shaped to at least 200 flakes, which has an approximate cost of ~$0.15 per device. The demonstrated cost-effective LIL patterning method has the potential to rapidly produce Bragg stacks at mass scale using a laser diode setup. These Bragg stacks may find a wide range of applications in disease diagnostics, toxicity detection, and drug discovery.

EXPERIMENTAL SECTION

Characterization of beetle elytra. Beetle elytra were treated by serial dehydration using ethanol and propylene oxide, and embedded within Epoxy. Ultrathin cross-sections of samples were utilized for SEM and TEM imaging. The diffraction spectra were measured using micro-spectrum analysis equipment with an aperture normal incidence at ~3°.

Modeling and fabrication of Bragg stacks. The AgBr NCs within hydrogel were simulated using a finite-element method. The Bragg stack sensor was fabricated by LIL combined with silver halide chemistry. Briefly, a monomer solution containing AM (77 mol%), PEGDA (3 mol%), 3-APBA (20 mol%), and 2-HMP in deionized (DI) water (2%, v/v) was pipetted on a silanized glass slide. The p(AM-*co*-PEGDA-*co*-3-APBA) hydrogel film was formed by UV exposure for 3 min. The unreacted monomers were removed from the hydrogel matrix by rinsing with ethanol and deionized (DI) water.[28] The Bragg stacks fabrication process was performed over eight steps. (1) AgNO$_3$ solutuon was diffused into the hydrogel film and dried

under a tepid air current; (2) The hydrogel film was treated with LiBr-acridine orange solution (photosensitization solution) for 40 s and rinsed with DI water. (3) The photosensitized hydrgel film was immersed in an ascorbate buffer and sandwiched with another clean glass slide. The sandwiched hydrogel film was placed on a leveled plane mirror and tilted 5° from the surface plane in Denisyuk reflection mode. (4) The hydrogel film was exposed to the laser light (λ=532 nm, 5 mW) for 10 s under red safe lighting to form a latent image of a multilayer stack. (5) The hydrogel film was immersed in a neutral photographic developer consisting of 2, 4-diaminophenol dihydrochloride (75 mmol L^{-1}), sodium sulfite (125 mmol L^{-1}) and sodium carbonate (65 mmol L^{-1}) for 1 min. (6) The hydrogel film was submerged in a stop bath containing acetic acid (2 vol%) for 1 min to stop the action of the developer. (7) The unexposed AgBr NCs within the film were removed by a hypo solution containing sodium thiosulfate (0.6 mol L^{-1}) for 10 min. (8) The Bragg stacks were submerged in an anti-printout solution containing sodium persulfate (0.8 mol L^{-1}) and sodium hydrogen sulphate (0.3 mol L^{-1}) for 3 min.

Glucose sensing by Bragg peak shift measurement. Glucose (100 mmol L^{-1}) and glucose-free solutions in PBS (pH 7.4) were mixed to prepare concentrations ranging from 5 to 20 mmol L^{-1}. Bragg stack hydrogel film was placed in a cuvette containing glucose solutions. The measurement was performed using a spectrophotometer under broadband light. The diffraction spectra from the spectrophotometer were recorded at 5 min time intervals.

Supporting Information
Supporting Information is available from the Wiley Online Library or from the author.

References

[1] P. Vukusic, J. R. Sambles, *Nature* **2003**, 424, 852.

[2] a) J. Sun, B. Bhushan, J. Tong, *RSC Adv.* **2013**, 3, 14862; b) J. P. Vigneron, J. M. Pasteels, D. M. Windsor, Z. Vértesy, M. Rassart, T. Seldrum, J. Dumont, O. Deparis, V. Lousse, L. P. Biró, *Phys. Rev. E* **2007**, 76, 031907; c) D. Stuart-Fox, A. Moussalli, *Phil. Trans. R. Soc. B* **2009**, 364, 463.

[3] L. Mäthger, M. Land, U. Siebeck, N. Marshall, *J. Exp. Biol.* **2003**, 206, 3607.

[4] a) H. Hinton, G. Jarman, *Nature* **1972**, 238, 160; b) H. Hinton, G. Jarman, *J. Insect Physiol.* **1973**, 19, 533541.

[5] J. Teyssier, S. V. Saenko, D. Van Der Marel, M. C. Milinkovitch, *Nat. Commun.* **2015**, 6.

[6] T. Lu, W. Peng, S. Zhu, D. Zhang, *Nanotechnology* **2016**, 27, 122001.

[7] a) F. Liu, B. Dong, X. Liu, Y. Zheng, J. Zi, *Opt. Express* **2009**, 17, 16183; b) H.-b. Seo, S.-Y. Lee, *Sci. Rep.* **2017**, 7, 44927.

[8] S. Kinoshita, S. Yoshioka, J. Miyazaki, *Rep. Prog. Phys.* **2008**, 71, 076401.

[9] J. Whittaker, *Biochim. Biophys. Acta* **1979**, 583, 378.

[10] Y. Yue, T. Kurokawa, M. A. Haque, T. Nakajima, T. Nonoyama, X. Li, I. Kajiwara, J. P. Gong, *Nat. Commun.* **2014**, 5, 4659.

[11] a) A. K. Yetisen, I. Naydenova, F. da Cruz Vasconcellos, J. Blyth, C. R. Lowe, *Chem. Rev.* **2014**, 114, 10654; b) K. Nonaka, *Appl. Opt.* **1997**, 36, 4792.

[12] a) K. Sano, Y. S. Kim, Y. Ishida, Y. Ebina, T. Sasaki, T. Hikima, T. Aida, *Nat. Commun.* **2016**, 7, 12559; b) L. Phan, R. Kautz, E. M. Leung, K. L. Naughton, Y. Van Dyke, A. A. Gorodetsky, *Chem. Mater.* **2016**, 28, 6804.

[13] M. Xiao, Y. Li, J. Zhao, Z. Wang, M. Gao, N. C. Gianneschi, A. Dhinojwala, M. D. Shawkey, *Chem. Mater.* **2016**, 28, 5516.

[14] a) C. Zhang, G. G. Cano, P. V. Braun, *Adv. Mater.* **2014**, 26, 5678; b) Y. Y. Diao, X. Y. Liu, G. W. Toh, L. Shi, J. Zi, *Adv. Funct. Mater.* **2013**, 23, 5373; c) M. Chen, L. Zhou, Y. Guan, Y. Zhang, *Angew. Chem. Int. Ed.* **2013**, 52, 9961; d) Y. Kang, J. J. Walish, T. Gorishnyy, E. L. Thomas, *Nat. Mater.* **2007**, 6, 957.

[15] a) Z. Cai, D. H. Kwak, D. Punihaole, Z. Hong, S. S. Velankar, X. Liu, S. A. Asher, *Angew. Chem. Int. Ed.* **2015**, 54, 13036; b) Z. Cai, L. A. Luck, D. Punihaole, J. D. Madura, S. A. Asher, *Chem. Sci.* **2016**, 7, 4557.

[16] a) M. Deubel, G. Von Freymann, M. Wegener, S. Pereira, K. Busch, C. M. Soukoulis, *Nat. Mater.* **2004**, 3, 444; b) A. Selimis, V. Mironov, M. Farsari, *Microelectron. Eng.* **2015**, 132, 83; c) J.-H. Seo, J. H. Park, S.-I. Kim, B. J. Park, Z. Ma, J. Choi, B.-K. Ju, *J. Nanosci. Nanotechnol.* **2014**, 14, 1521.

[17] S. Zhu, Y. Fu, J. Hou, *Lithography: Principles, processes and materials*, Nova Science Publishers, Hauppauge, NY, U.S.A. **2011**.

[18] a) Y. Montelongo, A. K. Yetisen, H. Butt, S.-H. Yun, *Nat. Commun.* **2016**, 7, 12002; b) A. K. Yetisen, Y. Montelongo, F. da Cruz Vasconcellos, J. Martinez-Hurtado, S. Neupane, H. Butt, M. M. Qasim, J. Blyth, K. Burling, J. B. Carmody, *Nano Lett.* **2014**, 14, 3587.

[19] Thorlabs, NPL52B - Nanosecond Pulsed Laser Diode System, 520 nm, 5 - 39 ns Adjustable Pulse Width. https://www.thorlabs.com/, accessed: August 1, 2017.

[20] L. Li, J. T. Fourkas, *Mater. Today* **2007**, 10, 30.

[21] W.-C. Su, K.-T. Kuo, presented at Microoptics Conference (MOC), 20th, Fukuoka, Japan **2015**.

[22] A. K. Yetisen, Y. Montelongo, M. M. Qasim, H. Butt, T. D. Wilkinson, M. J. Monteiro, S. H. Yun, *Anal. Chem.* **2015**, 87, 5101.

20

[23] S. A. Benton, V. M. Bove, in *Holographic Imaging*, Wiley-Interscience, Hoboken, N.J. **2007**, p. 173.

[24] R. Gurney, N. Mott, *Proc. R. Soc. A* **1938**, 164, 151.

[25] C. P. Tsangarides, A. K. Yetisen, F. da Cruz Vasconcellos, Y. Montelongo, M. M. Qasim, T. D. Wilkinson, C. R. Lowe, H. Butt, *RSC Adv.* **2014**, 4, 10454.

[26] E. V. Tan, C. R. Lowe, *Anal. Chem.* **2009**, 81, 7579.

[27] A. K. Yetisen, H. Butt, F. da Cruz Vasconcellos, Y. Montelongo, C. A. Davidson, J. Blyth, L. Chan, J. B. Carmody, S. Vignolini, U. Steiner, *Adv. Opt. Mater.* **2014**, 2, 250.

[28] A. K. Yetisen, N. Jiang, A. Fallahi, Y. Montelongo, G. U. Ruiz‑Esparza, A. Tamayol, Y. S. Zhang, I. Mahmood, S. A. Yang, K. S. Kim, H. Butt, A. Khademhosseini, S.-H. Yun, *Adv. Mater.* **2017**, 29, 1606380.

[29] D. Lee, M. S. Taylor, *J. Am. Chem. Soc.* **2011**, 133, 3724.

[30] T. D. James, K. S. Sandanayake, R. Iguchi, S. Shinkai, *J. Am. Chem. Soc.* **1995**, 117, 8982.

[31] Y. Guan, Y. Zhang, *Chem. Soc. Rev.* **2013**, 42, 8106.

[32] V. L. Alexeev, A. C. Sharma, A. V. Goponenko, S. Das, I. K. Lednev, C. S. Wilcox, D. N. Finegold, S. A. Asher, *Anal. Chem.* **2003**, 75, 2316.

[33] H. Li, *Smart Hydrogel Modelling*, Springer Science & Business Media, Heidelberg, Germany **2010**.

[34] W. Zhai, X. Sun, T. D. James, J. S. Fossey, *Chem. Asian J.* **2015**, 10, 1836.

[35] a) W. K. Smothers, B. M. Monroe, A. M. Weber, D. E. Keys, *Practical Holography IV* **1990**, 1212, 20; b) S. Paul, I. Vartiainen, M. Roussey, T. Saastamoinen, J. Tervo, S. Honkanen, M. Kuittinen, *Opt. Express* **2016**, 24, 26901.

[36] M. Bruening, D. Dotzauer, *Nat. Mater.* **2009**, 8, 449.

[37] a) X. Yang, M. C. Lee, F. Sartain, X. Pan, C. R. Lowe, *Chem. Eur. J.* **2006**, 12, 8491; b) S. Kabilan, J. Blyth, M. Lee, A. Marshall, A. Hussain, X. P. Yang, C. Lowe, *J. Mol. Recogn.* **2004**, 17, 162; c) W. Zhai, B. M. Chapin, A. Yoshizawa, H.-C. Wang, S. A. Hodge, T. D. James, E. V. Anslyn, J. S. Fossey, *Org. Chem. Front.* **2016**, 3, 918; d) W. Zhai, L. Male, J. S. Fossey, *Chem. Commun.* **2017**, 53, 2218; e) D. H.-C. Chou, M. J. Webber, B. C. Tang, A. B. Lin, L. S. Thapa, D. Deng, J. V. Truong, A. B. Cortinas, R. Langer, D. G. Anderson, *Proc. Natl. Acad. Sci.* **2015**, 112, 2401.

[38] J.-T. Zhang, Z. Cai, D. H. Kwak, X. Liu, S. A. Asher, *Anal. Chem.* **2014**, 86, 9036.

[39] a) Q. Zhang, B. Chen, L. Tao, M. Yan, L. Chen, Y. Wei, *RSC Adv.* **2014**, 4, 32475; b) Z. Liu, W. Wang, R. Xie, X.-J. Ju, L.-Y. Chu, *Chem. Soc. Rev.* **2016**, 45, 460; c) X. Hou, W. Guo, L. Jiang, *Chem. Soc. Rev.* **2011**, 40, 2385.

[40] J. D. Newman, A. P. Turner, *Biosens. Bioelectron.* **2005**, 20, 2435.

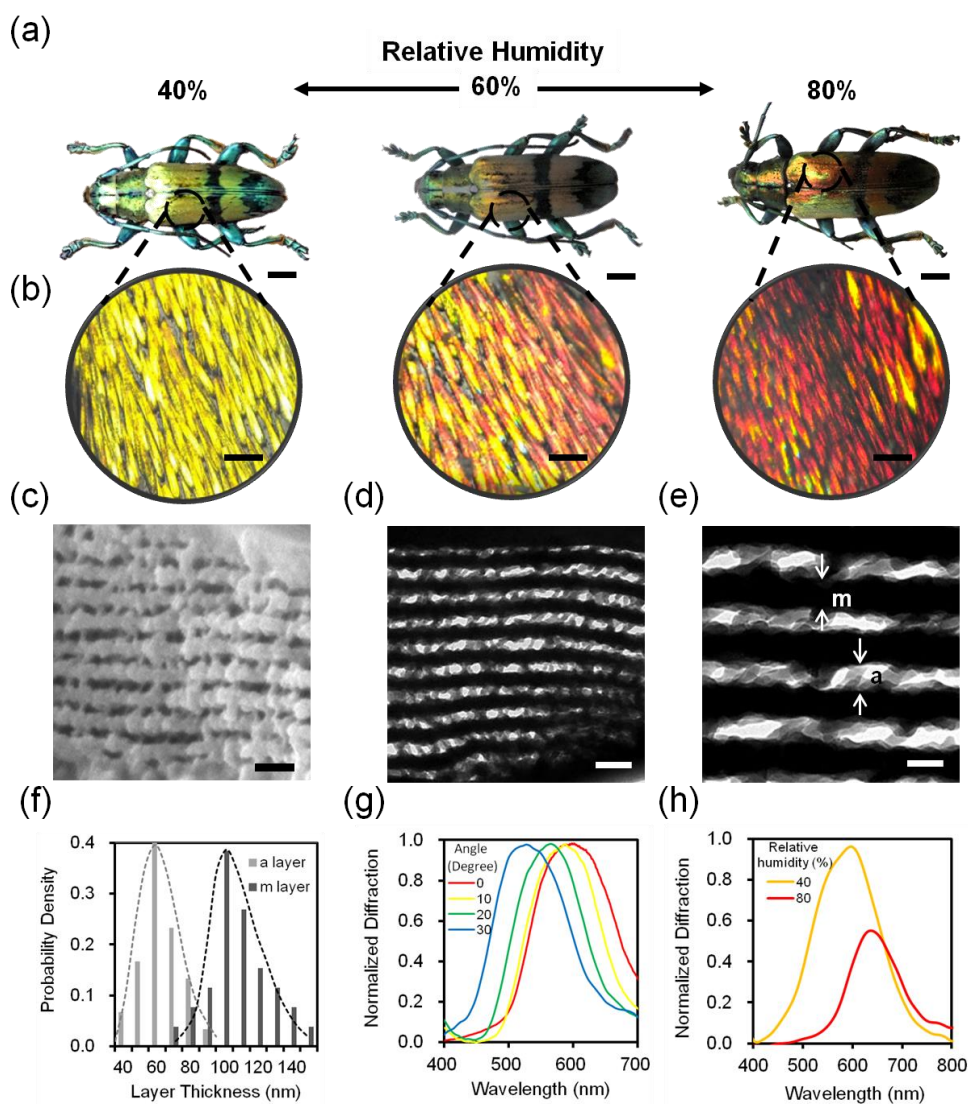[41] P. J. Flory, *Principles of polymer chemistry*, Cornell University Press, Ithaca, NY, **1953**.

Figure 1. Structural color changes of the *Tmesisternus isabellae* elytra stimulated by humidity. (a) Photographs of color changes of beetle elytra in low (40%), interim (60%), high (80%) relative humidities. Scale bar= 2.0 mm. (b) Optical microscopy images of color changes of the elytra under broadband light in different humidity conditions. Scale bar= 50 μm. (c) Transverse cross-section SEM image of elytra. Scale bar= 500 nm. (d) Transverse cross-section TEM image of the elytra showing a Bragg stack structure. Scale bar= 400 nm. (e) Magnified TEM image of the Bragg stack structure. The "m" and "a" layers represent the melanoprotein layer and the air gap layer, respectively. Scale bar= 200 nm. (f) Melanoprotein and air layer thickness distributions in the elytra. (g) Angle-resolved measurements of the beetle elytra. (h) Normalized diffraction spectra of the elytra in low (40%) and high (80%) relative humidity conditions.
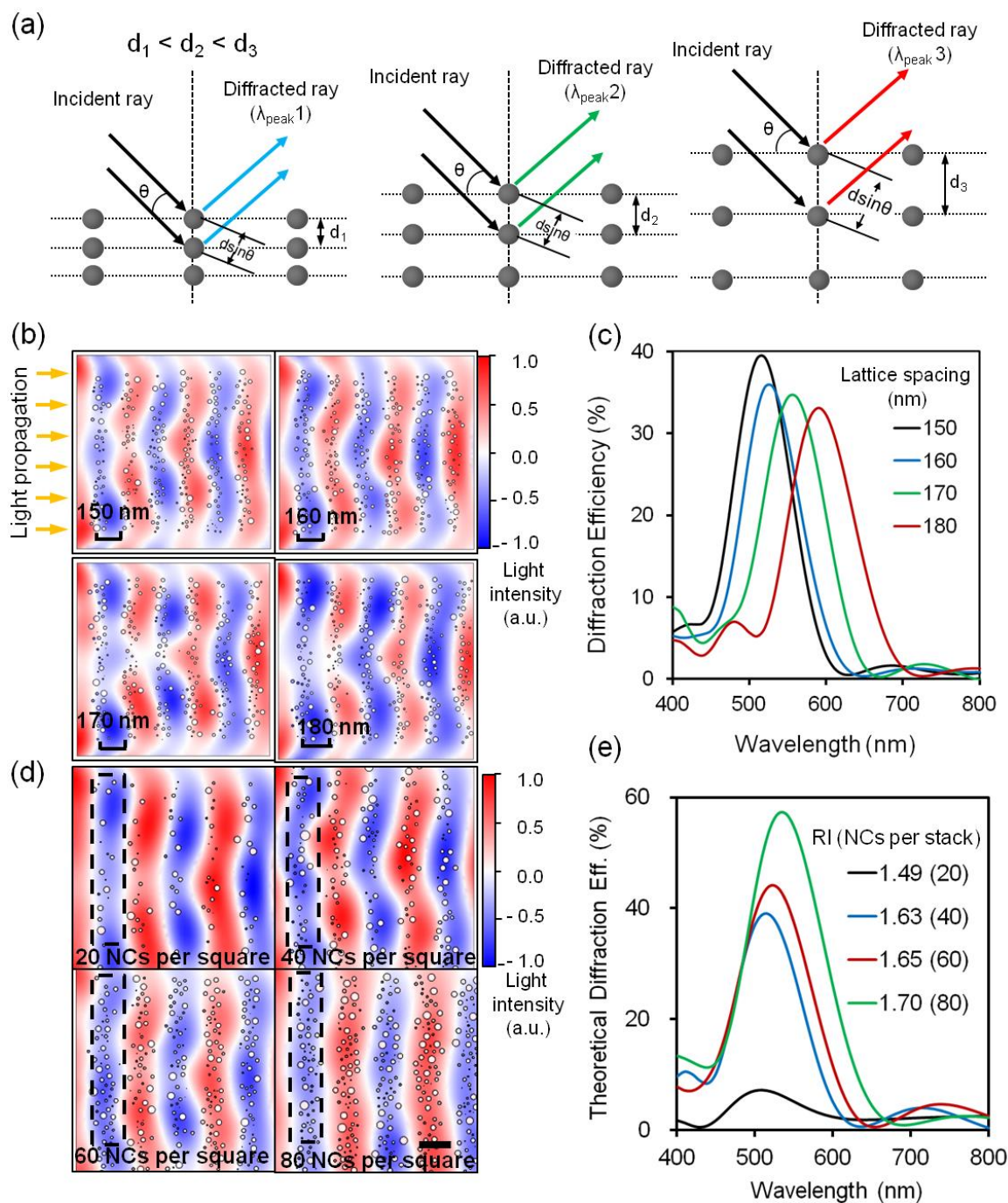
Figure 2. Finite-element simulations of tunable Bragg stacks. (a) Expansion of lattice spacing in a Bragg stack shifts the diffracted ray to longer wavelengths. (b) Simulated geometries and wave propagation results for the Bragg diffracted waves of the multilayered structures. (c) The simulated diffraction spectra for different lattice spacings. (d) Simulated geometries and wave propagation results for different effective RIs (AgBr NC density) of the Bragg stacks. Scale bar=150 nm. Dashed areas show counted nanoparticles per stack. (e) The simulated diffraction spectra for different effective RI values within the Bragg stacks.
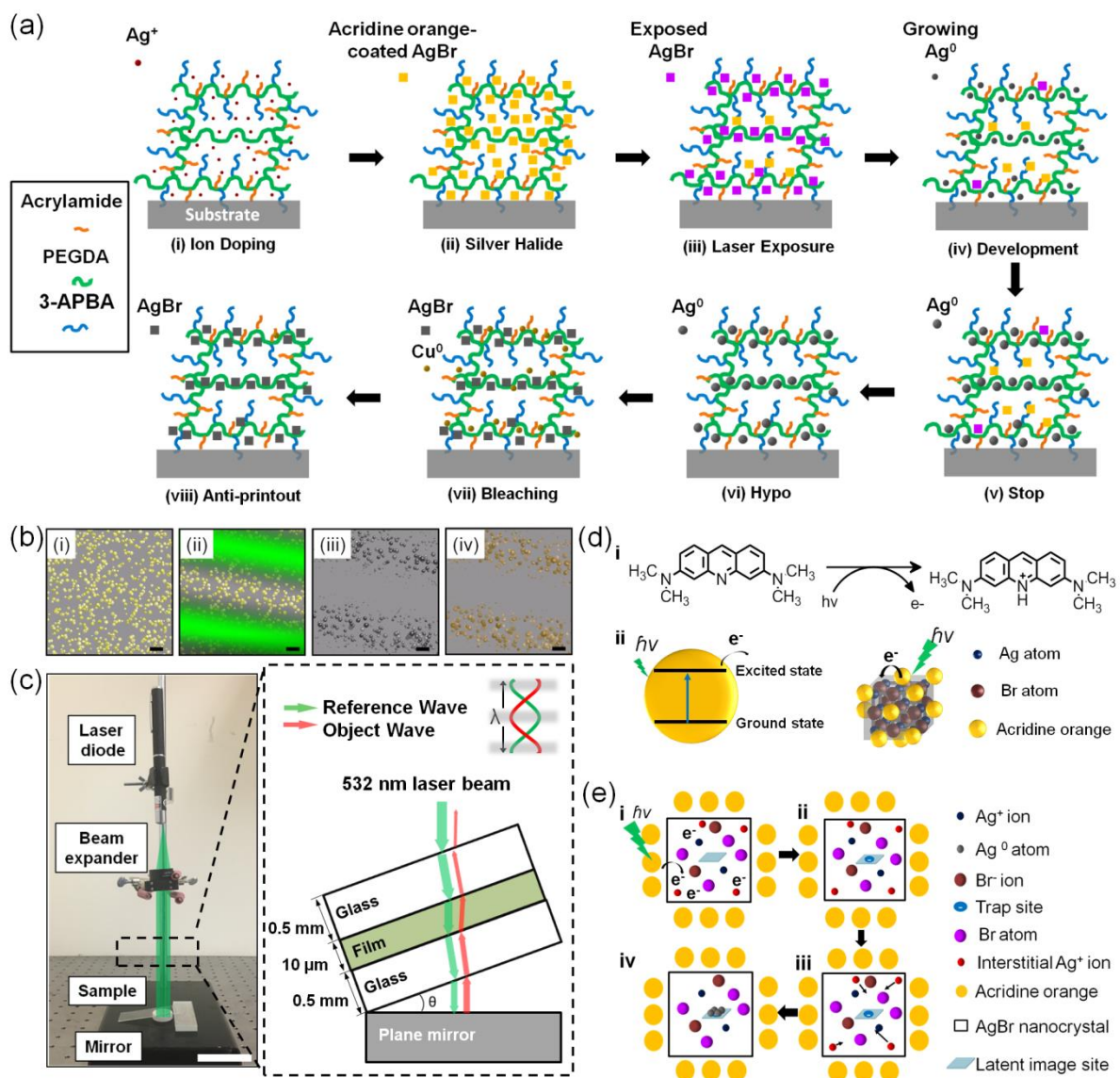
Figure 3. Fabrication of a Bragg stack using LIL in hydrogel films. (a) Formation of a latent image and grating in silver halide chemistry. (i) Ag$^+$ ions (AgNO$_3$, 100 mmol L^{-1}) were diffused into the hydrogel film, (ii) AgBr NC formation, (iii) latent image formation, (iv) the reduction of AgBr NCs to Ag^0 NPs using a neutral developer, (v) stop bath, (vi) hypo to remove undeveloped AgBr NCs, (vii) bleaching solution to convert Ag^0 NPs to AgBr NCs, and (viii) anti-printout bath to etch Cu^0 NPs. (b) Simulation of AgBr NC growth within the light inference domain in Denisyuk reflection mode. (i) Formation of photosensitive AgBr NCs distributed within the hydrogel film, (ii) creation of the latent image under the laser exposure; (iii) formation of multilayers consisting of Ag^0 NP stack, (iv) Bragg stacks having multilayer AgBr NCs. Scale bar= 30 nm, (c) Denisyuk reflection mode was setup to record a

24

latent image using a CW laser diode (λ=532 nm, 5.0 mW). Scale bar=5.0 cm. The inset shows standing wave formation. (d) Energy transfer between acridine orange and AgBr NCs. (e) Latent image formation in AgBr NCs: (i) absorption of a photon and electron transfer from acridine orange to the AgBr NCs, (ii) formation of a negatively charged electron trap zone, (iii) the migration of interstitial Ag^+ ions to the trap zone, and (iv) the reduction of Ag^+ ions to Ag^0 atoms and formation of a Ag speck (latent image).
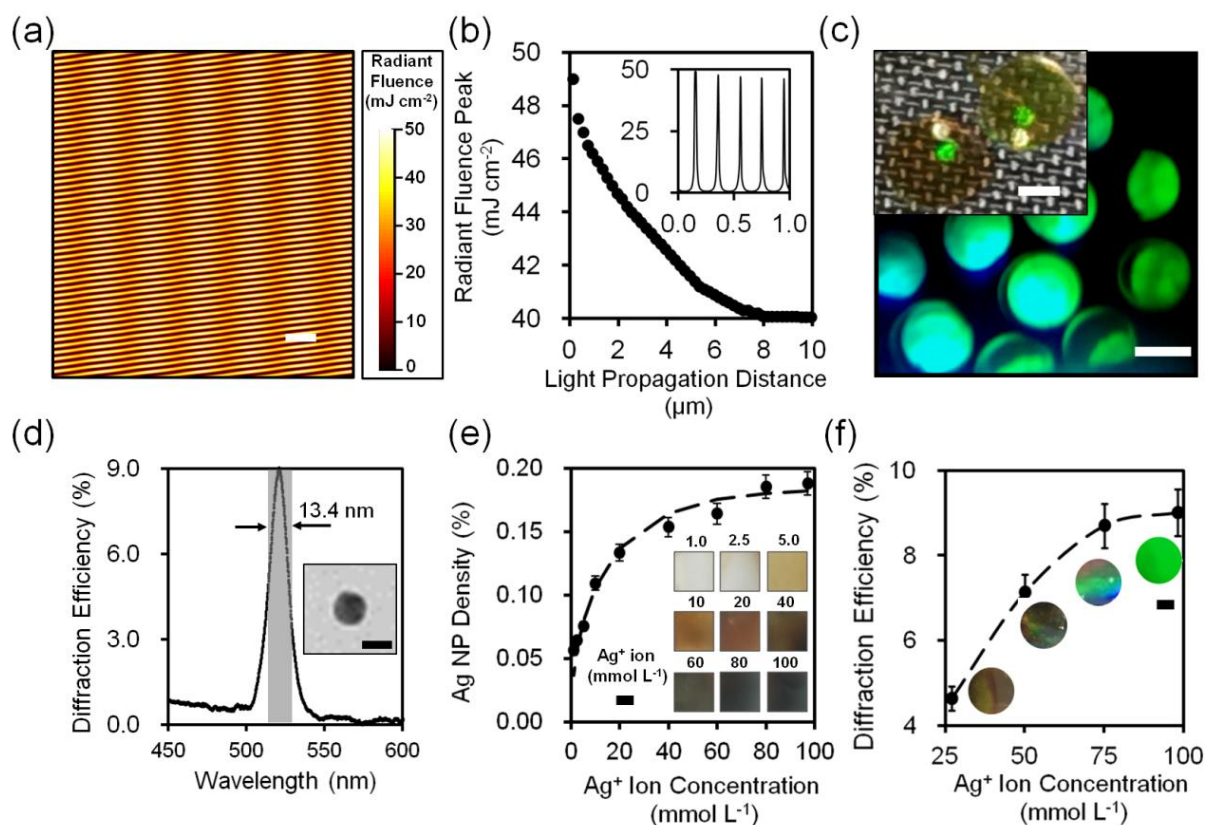
Figure 4. Characterization of the p(AM-*co*-PEGDA) Bragg stack films. (a) The field distribution generated by light interference within the hydrogel film with a tilt angle of 5°, created by two waves: reference wave and object wave. Scale bar=1.0 μm. (b) Laser light interference propagation within the the whole hydrogel matrix with a propagation distance of 10 μm. Peaks represent standing wave peak. Inset shows light interference propagation with a propagation distance of 1 μm. (c) A photograph of Bragg stacks produced by silver halide chemistry. Scale bar=200 μm. Inset shows a photograph of two substrate-free Bragg stack flakes. Scale bar=1 mm. (d) Diffraction spectrum. Inset shows a TEM image of an embedded single Ag^0 NP within hydrogel film. Scale bar=10 nm. (e) Ag^0 NPs density within hydrogel matrix. Insets show the photographs of hydrogel films loaded with different concentrations of Ag^0 NPs (n=3). Scale bar=2.0 mm. (f) The effect of Ag^+ ion concentration on diffraction efficiency of the Bragg stacks consisting of AgBr NCs (n=3). Inset shows the photographs of hydrogel films. Scale bar=2.0 mm. Error bars represent standard deviation.
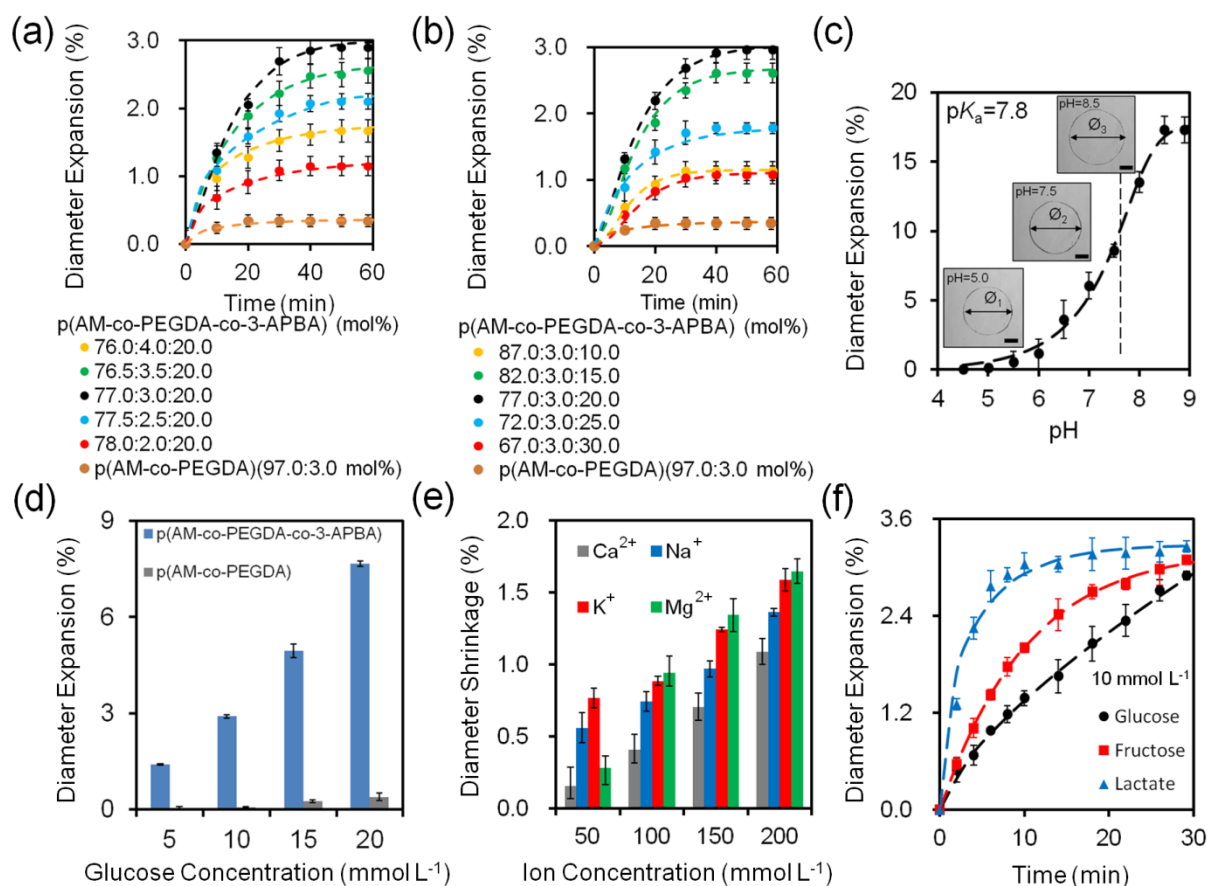
Figure 5. Quantification of glucose concentration with p(AM-*co*-PEGDA-*co*-3-APBA) film at pH 7.4 at 24 °C. The hydrogels were fully swollen during the measurements. (a) Time-lapse measurements of the expansion of hydrogel flake diameter (Ø=2 mm) by varying concentrations of PEGDA in the presence of glucose (10 mmol L^{-1}) and control experiments fitted with the exponential decay equation, where the decay constant α was 1.9×10^{-2} s^{-1} (n=3). (b) Time-lapse measurements of the expansion of hydrogel flake diameter (Ø=2 mm) by varying concentrations of 3-APBA in the presence of glucose (10 mmol L^{-1}) and control experiments fitted with the exponential decay equation (n=3). (c) pH-dependent hydrogel flake expansion (10 mmol L^{-1}) (n=3). $Ø_1$, $Ø_2$, and $Ø_3$ represent diameters at pH value of 5.0, 7.5 and 8.5, respectively. Scale bar=1.0 mm, the curve is fit to Equation 4. (d) The change in the diameter of the hydrogel flakes as the glucose concentration increasing from 5 to 20 mmol L^{-1} (n=3). (e) Ionic effect on hydrogel flake shrinkage (n=3). (f) Hydrogel flake response to glucose, fructose, and lactate (10 mmol L^{-1}) (n=3). Error bars represent standard deviation.
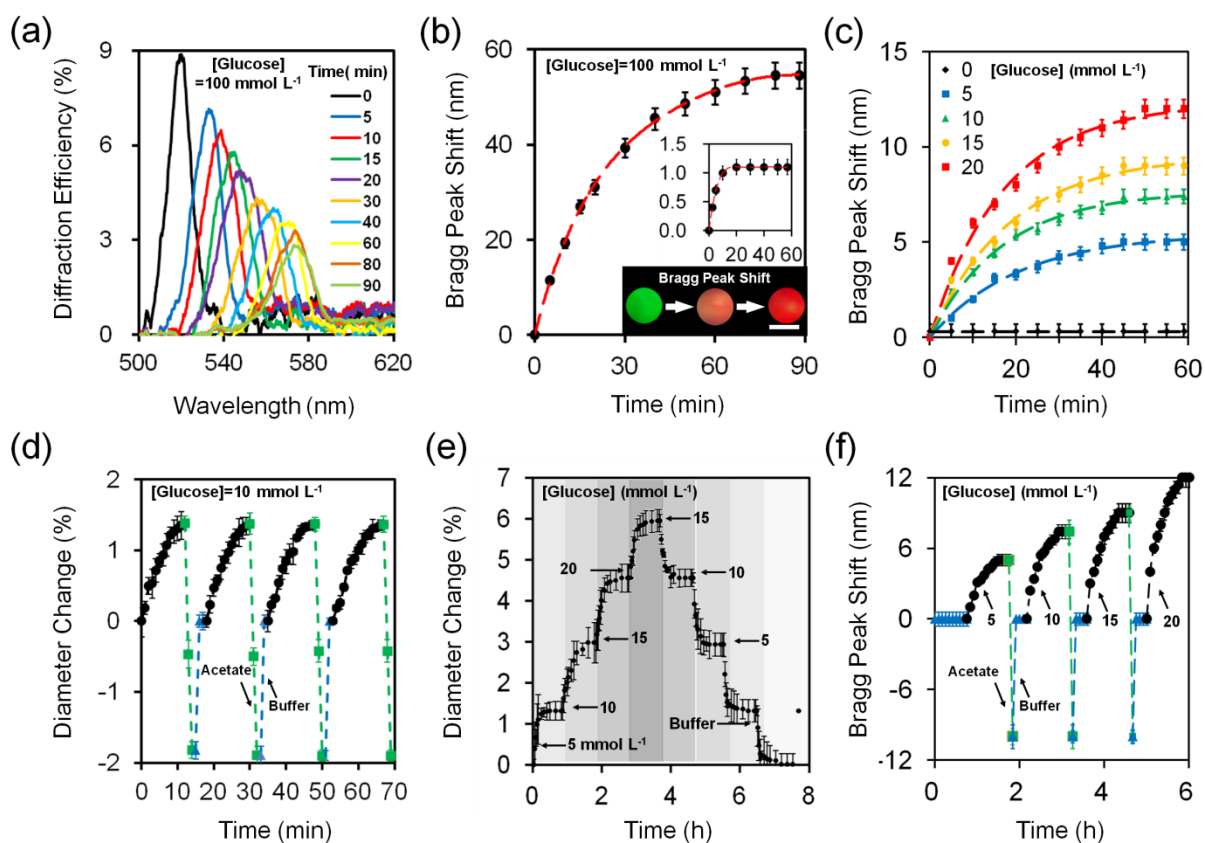
Figure 6. Quantifications of glucose concentrations and reversibility. (a) Diffraction spectra of a Bragg stack hydrogel film in response to glucose (100 mmol L^{-1}) over 90 min. The dash line was fitted using Equation 7, where the constants were c=99 nm, λ_0=452 nm, and I_0=−0.45. (b) The peak shift of the Bragg stacks as a function of time (n=3). Insets show colorimetric readouts of the Bragg stacks, and the control experiment without 3-APBA (n=3). Scale bar=2.0 mm. (c) Quantification of glucose by the Bragg stacks within the physiological glucose range (n=3). The dashed lines were fitted using Equation 7. (d) Reset experiment of the hydrogel flakes by varying glucose solution (10 mmol L^{-1}) and acetate buffer (pH=4.6) (n=3). The hydrogel flake diameter was returned to its original size by using acetate buffer, followed by buffer rinse. (e) Reversibility of the hydrogel film in glucose sensing (n=3). Arrows show applied glucose concentrations. (f) Reusability of the Bragg stacks responding to glucose in continuous measurements based on diffracted peak shifts (n=3). Arrows show applied glucose concentrations. Error bars represent standard deviation.

Laser-directed interference lithography involving silver halide chemistry is utilized as a facile and rapid nanofabrication technique to create a slanted Bragg stack consisting of silver bromide nanocrystals in a hydrogel film. The lattice spacing of the Bragg stacks can be modulated by external stimuli to obtain dynamic diffraction peak shifts. The functionalization of the hydrogel with phenylboronic acid enables reversible quantitative measurements of glucose.

Nan Jiang, Haider Butt, Yunuen Montelongo, Feng Liu, Samson Afewerki, Guo-Liang Ying, Qing Dai, Seok-Hyun Yun, and Ali K. Yetisen*

Laser Interference Lithography for the Nanofabrication of Stimuli-Responsive Bragg Stacks
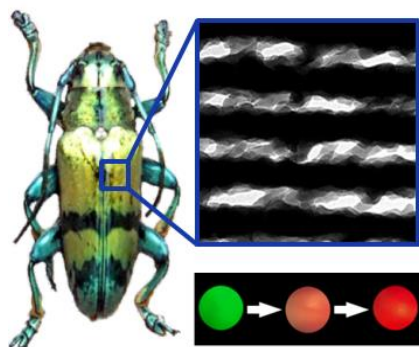
Supporting Information

Laser Interference Lithography for the Nanofabrication of Stimuli-Responsive Bragg Stacks

Nan Jiang, Haider Butt, Yunuen Montelongo, Feng Liu, Samson Afewerki, Guo-Liang Ying, Qing Dai, Seok-Hyun Yun, and Ali K. Yetisen*

EXPERIMENTAL SECTION

Materials. The longhorn beetles *Tmesisternus isabellae* were obtained from the Shanghai Natural History Museum (China). Acrylamide (AM, 99%), poly(ethylene glycol) diacrylate (PEGDA) (M_n=700 Da), 2-hydroxy-2-methylpropiophenone (2-HMP, 97%), 3-(acrylamido)phenylboronic acid (3-APBA, 98%), silver nitrate ($AgNO_3$, 99%), *N,N,N',N'*-tetramethylacridine-3,6-diamine (acridine orange, 75%), hydrogen peroxide (35 wt%), lithium bromide (LiBr, 99%), 3-(trimethoxysilyl)propyl methacrylate (98%), sodium L-ascorbate (98%), hydrochloric acid (37%), 2-4-diaminophenol dihydrochloride (amidol, 98%), sodium sulfite (98%), acetic acid (99%), sodium hydroxide (NaOH, 97%), sodium thiosulphate (99%), acetonitrile (99%), sodium carbonate (99%), acetate buffer (pH=4.6), copper sulfate (98%), ammonium persulfate (98%), sodium hydrogen sulphate (95%), D-(+)-glucose (99%), D-(−)-fructose (99%), sodium L-lactate (98%), Tween® 20, epoxy embedding medium, formic acid (95%), sodium chloride (99%), potassium chloride (99%), calcium chloride (99%), magnesium chloride (99%), trizma® hydrochloride (99%), trizma® base (99%), (±)-propylene oxide (99%) and PBS tablets (pH 7.4, 10 mmol L^{-1} phosphate buffer, 137 mmol L^{-1} NaCl and 2.7 mmol L^{-1} KCl) were purchased from Sigma Aldrich. Quetol 651 (epoxy resin) was

purchased from Electron Microscopy Sciences. Acetone (100%) and ethanol (100%) were purchased from Fisher Scientific.

Equipment. Ultrathin cross-section samples were cut using an ultramicrotome (Leica, EM UC6). The photographs of the beetle and Bragg stacks were captured using a digital single-lens reflex camera (12.3 MP) using a lens (AF-S DX 18-105 mm f/3.5-5.6G ED VR) operated at ISO H 1.0, 1/1500 speed, and F3.5 (Nikon, Japan). The microscopic images of beetle elytra were captured using a LYNX inspection optical microscope (Vision Engineering Co., UK). The morphology of elytra was characterized using a SEM (XL 30 FEG, Philips) and a TEM (JEM-1230, JEOL). Polyester sheets were purchased from Dura-Lar (USA). A refractometer (300053) was purchased from Sper Scientific (USA), copper grids (200 mesh and 400 mesh) were purchased from Sigma-Aldrich. The hydrogel films were crosslinked by exposing under a UV light source (λ=365 nm, 5 mW cm^{-2}, Spectroline). Diffraction spectra of elytra were obtained using a microspectra analysis equipment consisting of a microscope (Leica DM6000 M) integrated with a tungsten light source and an optical spectrometer (Spectra Pro 500i, Action Research Co., USA). A portable laser pointer (532 nm, 5 mW) was purchased from Digikey. Diffraction spectra of Bragg stacks were measured using a spectrophotometer (Thorlabs CCS100, 350-700 nm) equipped with a broadband white light source, an optical lens (f=2.54 cm), and a plane mirror.

Sampling beetle elytra for electron microscopy. Beetle elytra were cut and incubated in a solution containing NaOH (250 mmol L^{-1}) and Tween-20 (0.1 vol%) for 30 min. The samples were treated with formic acid and ethanol (2:3, v/v), followed by dehydration using ethanol and ($\pm$)-propylene oxid. Epoxy was infiltrated to embed the samples. Ultrathin cross-sections were cut using a diamond knife on an ultramicrotome and placed on a 200 mesh copper grid.

Bleaching test of elytra. Beetle elytra were immersed in hydrogen peroxide (20 wt%) for 24 h. The color of beetle elytra was observed under microscope using reflection and transmission modes.

Diffraction spectra measurement of beetle elytra. The diffraction spectra were measured using a microspectra analysis equipment. During the measurements, a circular diaphragm (Ø=0.5 mm) was applied to create a narrow aperture normal incidence (~3°). A broadband metallic flat mirror (PYREX, USA) was used as a reference.

Modeling of the Bragg stacks. Multilayer structures were modeled using a finite-element method in COMSOL Multiphysics. The AgBr NCs (RI, *n*=2.26) were generated using a MATLAB code, in which the sizes of grains were 4-24 nm (σ=5 nm). The effective RI of the surrounding area was defined as 1.38 corresponding to the RI of p(AM-*co*-PEGDA) hydrogel measured by a refractometer. The mesh size was ~2 nm to resolve each AgBr NC. The number of AgBr NCs per stack was 20-80 and the lattice spacing was varied from 150 to 180 nm. Broadband light (400-800 nm) was propagated through a square domain (2.5×2.5 μm^2) consisting of stacked layers of AgBr NCs. Upon illumination of the Bragg stack normally, the diffracted light was collected through a parametric sweep.

Silanization of glass slides. A silane solution consisting of 3-(trimethoxysilyl)propyl methacrylate solution dissolved in acetone (v/v, 1:50) was prepared. Glass slides (2.5×3.5×1.0 cm^3) were immersed in the silane solution in an aluminum tray for 1 min, and excess saline solution was removed. The slides were kept at 24 °C for 12 h in the dark. The slides were rinsed with ethanol and stored in the dark.

Synthesis of p(AM-co-PEGDA) Films. A monomer solution containing AM (77 mol%), PEGDA (3 mol%), 3-APBA (20 mol%), and 2-HMP in deionized (DI) water (2%, v/v) was filtered (pore diameter, Ø=0.22 μm) and pipetted as an elongated blob onto a polyester sheet, where a silanized glass slide was placed on the blob. Exposing the monomer solution to UV light (λ=365 nm, 5 mW cm^{-2}) for 3 min formed a p(AM-*co*-PEGDA-*co*-3-APBA) film on the glass slide. The crosslinked hydrogel film was rinsed with ethanol and deionized (DI) water (v/v, 1:1) to remove excess monomers.

Photosensitization of p(AM-co-PEGDA) Films. Experiments were performed under red safe lighting in a darkroom. $AgNO_3$ (0.1 mol L^{-1}, 200 μL) solution was pipetted onto the hydrogel film and diffused for 3 min, followed by drying the hydrogel film under a tepid air current for 5 s. A photosensitization solution was prepared by mixing (v/v, 50:1) LiBr (0.3 mol L^{-1}) with acridine orange dye (15 mmol L^{-1}, dissolved in ethanol/water, v/v, 1:1). The hydrogel film was immersed in the LiBr-acridine orange solution for 40 s to form AgBr NCs within the hydrogel film, followed by rinsing with DI water.

Latent Image Formation in p(AM-co-PEGDA) Films. The photosensitized hydrogel films were soaked in ascorbate buffer (pH ~6.0) and sandwiched using a glass slide. The sandwiched system was placed on a leveled plane mirror and tilted 5° from the surface plane in Denisyuk reflection mode. The optical table was stabilized for 1 min to minimize environmental vibration. The hydrogel film was exposed to the laser light (λ=532 nm, 5 mW) for 10 s under red safe lighting to form a latent image of a multilayer stack.

Formation of Bragg Stacks in p(AM-co-PEGDA) Films. A neutral photographic developer consisting of 2, 4-diaminophenol dihydrochloride (75 mmol L^{-1}), sodium sulfite (125 mmol L^{-1}) and sodium carbonate (65 mmol L^{-1}) in DI water was prepared. The hydrogel film was immersed in the developer for 1 min to convert the latent image in AgBr NCs to Ag^0 NPs. The hydrogel film was submerged in a stop bath containing acetic acid (2 vol%) for 1 min to stop the action of the developer.

Post-treatment of Bragg Stacks. To remove the unexposed AgBr NCs, the hydrogel film was immersed in a hypo solution containing sodium thiosulfate (0.6 mol L^{-1}) for 10 min. Bragg stacks were bleached by immersing the hydrogel film into a solution containing copper sulphate (125 mmol L^{-1}), ammonium bromide (0.8 mol L^{-1}), and acetic acid (7 vol%) for 30 s. After rinsing the sample with DI water, the samples were submerged in an anti-printout solution containing sodium persulfate (0.8 mol L^{-1}) and sodium hydrogen sulphate (0.3 mol L^{-1}) for 3 min.

Transmission Electron Microscopy (TEM) Analysis of Ag^0 Nanoparticles in Hydrogels. The Ag^0 NPs embedded hydrogel films were subtracted from their substrates using a blade and moved to ethanol. The solution was replaced two times with acetonitrile incubating each replacement for 10 min. The samples were transferred to a mixture consisting of Quetol 651 and acetonitrile (1:1, v/v). The acetonitrile was allowed to evaporate for 12 h. The hydrogel films were transferred through Quetol 651 for 2 h each and the resin was cured at 60 °C for 2 days. Vertical sections through the hydrogel film were cut with a diamond knife equipped microtome. The hydrogel films were mounted on 400 mesh copper grids and observed in a TEM (120 kV, FEI Tecnai G2, Oregon, USA).

Preparation of Glucose, Fructose, Lactate, and Metal Ions Solutions. Glucose solution (5, 10, 15, 20 mmol L^{-1}) was prepared by dissolving D-(+)-glucose in Tris buffer (150 mmol L^{-1}, pH=7.4) at 24 °C. All the experiments were carried out at 24 °C. The glucose solution was serially diluted with the Tris buffer solution to achieve different concentrations (5, 10, 15, 20 mmol L^{-1}). Tris HCl (150 mmol L^{-1}) and Tris base (150 mmol L^{-1}) solutions were mixed to prepare a buffer solution with a pH value ranging from 4.5 to 9.0. Metal ion solutions were prepared from NaCl, KCl, $CaCl_2$ and $MgCl_2$ and were serially diluted with Tris buffer (pH7.4) to obtain different metal ion concentrations (50, 100, 150 and 200 mmol L^{-1}). Fructose and lactate solutions (10 mmol L^{-1}) were prepared by dissolving D-(-)-fructose and sodium-L-lactate in Tris buffer solution (pH=7.4).

Hydrogel Expansion in Response to Glucose. The hydrogel flakes with different concentrations of PEGDA and 3-APBA were fully swollen in Tris buffer solution (pH=7.4) at 24 °C prior to use. The buffer solution was replaced with glucose solution (10 mmol L^{-1}) in a 12 microwell culture plate and the hydrogel flake diameter was recorded using an optical microscope (2× objective) with 5 min time intervals over 1 h. For the measurement of the hydrogel flake expansion in different glucose solutions, the Tris buffer was replaced with glucose solutions (5-20 mmol L^{-1}). The diameter of the expansion was recorded over 40 min

and the hydrogel flake was rinsed with acetate buffer (pH=4.6) and Tris buffer solution (pH=7.4).

pK$_a$ Measurements of the Hydrogel Flakes. The hydrogel flake was immersed in Tris buffer solution (pH=4.5) and the diameter changes were measured and recorded over 30 min. The subsequent measurements were carried out by replacing Tris buffer solutions from the lower to higher pH solutions.

Reversibility of the Bragg stack. The glucose solutions were replaced with acetate buffer solutions to release the binding glucose molecules from the hydrogel. For reusability, the Tris buffer solutions were replaced with increased concentrations of glucose from 5 to 20 mmol L^{-1} and decreased concentrations from 20 mmol L^{-1} to glucose-free solution.

Bragg Peak Shift Measurements. Glucose (100 mmol L^{-1}) and glucose-free solutions in PBS (pH 7.4) were mixed to prepare concentrations ranging from 5 to 20 mmol L^{-1}. Bragg stack hydrogel film was placed in a cuvette, which contained glucose solutions (5-100 mmol L^{-1}) at 24 °C. The diffraction peak measurements of the Bragg stacks were performed using a setup including a broadband light source and a spectrophotometer connected to an optical fiber probe. The diffraction spectra from the spectrophotometer were recorded at 5 min time intervals. The images of the Bragg gratings corresponding to diffraction spectra of concentration measurements were captured by a bifurcated fiber and a digital camera. The peak of the Bragg stacks was reset to its original position using acetate buffer (pH=4.6).

Composition of Bragg stacks. Acrylamide (AM) (77 mol%), poly(ethylene glycol) diacrylate (PEGDA) (3 mol%), 3-(acrylamido)phenylboronic acid (20 mol%) were used to prepared hydrogel film. The solution was mixed with the ratio of 2:3 (w/v) with 2-hydroxy-2-methylpropiophenone (2-HMP) (2 vol%). Required calculation: A total of 5 mmol L^{-1} of monomer solution was used. AM, M × mw=3.85 mmol × 71.08 g mol^{-1}=0.274 g; PEGDA, M × mw=0.15 mmol×700 g mol^{-1}=0.105g; 3-APBA, M × mw=1.0 mmol × 190.90 g mol^{-}

[1]=0.190 g. AM to 2-HMP ratio is 2:3 (w/v) and we added 416 μL 2-HMP (2 vol%) in DI water. Total volume of the solution is ~510 μL. The mixed heterogeneous monomer solution was filtered through 0.45 μm pores.
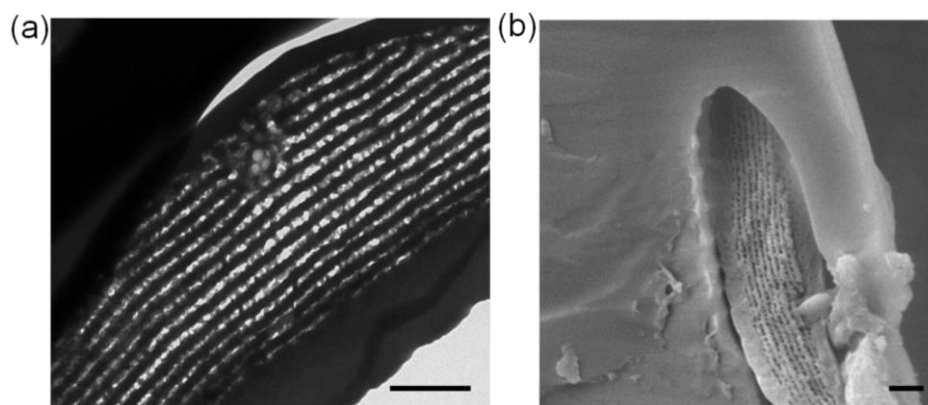
Table S1. Components of p(AM-*co*-PEGD-*co*-3-APBA) hydrogel.

Substance	Mw (g mol^{-1})	Amount of substance (mmol)	Weight (g)
AM	71.08	3.85	0.274
PEDGA	700	0.15	0.105
3-APBA	190.9	1.0	0.190

For a Bragg stacks, 200 μL solution was required to form a thickness ~10 μm hydrogel film on a silanized glass substrate (treated with 3-(trimethoxysilyl)propyl methacrylate TMOSPMA, 1 vol% in acetone). 400 μL silver nitrate ($AgNO_3$) solution (0.1 mol L^{-1}) was diffused to the hydrogel film. 1.3 g lithium bromide (LiBr) powder in 50 mL DI water, followed by adding 1 mL acridine orange dye (0.4 wt% in 100 mL (1:1 v/v ethanol to water)) in the bromide solution. 50 μL ascorbate buffer (100 mmol L^{-1}) was sandwiched between hydrogel film and a glass slide. The film was exposed under a portable laser pointer. The Bragg stack was formed by using a neutral developer (50 mL DI water containing 0.5 g 2, 4-diaminophenol dihydrochloride (Amidol), 0.5 g sodium sulfite (Na_2SO_3), 0.25 g sodium carbonate (Na_2CO_3)) and stop bath (2 vol% acetic acid). The film was washed in 50 mL Hypo solution (10% sodium thiosulphate). For bleaching process, the film was immersed in bleaching bath containing copper sulphate ($CuSO_4$, 2 wt%), lithium bromide (LiBr, 8 wt%) and acetic acid (7 vol%). An anti-printout solution was used for copper etching, which contains ammonia persulfate (($NH_4)_2S_2O_8$, 4 wt%) and sodium hydrogen sulphate ($NaHSO_4$, 4 wt%).

Table S2. Components of p(AM-*co*-PEGD-*co*-3-APBA) for a microscope slide grating.

Material	Mw (g mol^{-1})	Concentration	Req. amount	Cost ($)
2-HMP	164.2	2/3 (w/v) in DI	3.3 μL	0.01
TMOSPMA	248.4	1 vol%	0.2 mL	0.08
Acetone	58.1	49 vol%	9.8 mL	0.70
AgNO$_3$	169.9	100 mmol L^{-1}	0.0068 g	0.03
LiBr	86.9	0.3 mol L^{-1} and 8 wt%	1.3 g	1.98
Acridine orange dye	265.4	0.4 wt%	0.008 g	0.07
ethanol	46.1	50 vol%	1 mL	0.13
Na ascorbate buffer	198.1	100 mmol L^{-1}	9.9 ×10^{-4} g	0.01
Amidol	197.1	1 wt%	0.5 g	0.90
Na$_2$SO$_3$	126.0	1 wt%	0.5 g	0.07
Na$_2$CO$_3$	106.0	0.5 wt%	0.25 g	0.04
Acetic acid	60.1	2 vol%	2.25 mL	0.81
Na$_2$S$_2$O$_3$	158.1	10 wt%	0.25 g	0.06
CuSO$_4$	159.6	2 wt%	0.5 g	3.02
(NH$_4$)$_2$S$_2$O$_8$	228.2	4 wt%	1 g	1.13
NaHSO$_4$	120.1	4 wt%	1. g	0.09
Laser pointer				4.00
Lens				5.30
Mirror				6.00
Total price ($)	28.28			

Figure S1. Characterization of cross-section of beetle elytra. (a) TEM image of the elytra.

Scale bar=2 μm. (b) SEM image. Scale bar=1 μm.
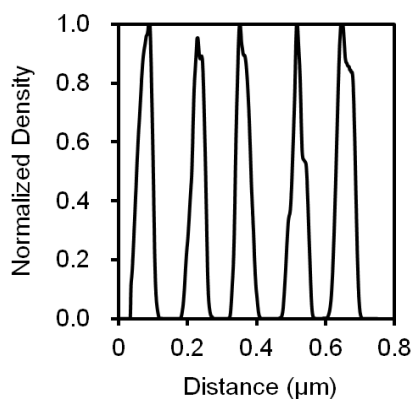
Figure S2. Alternating layer intensity distribution of beetle elytra.
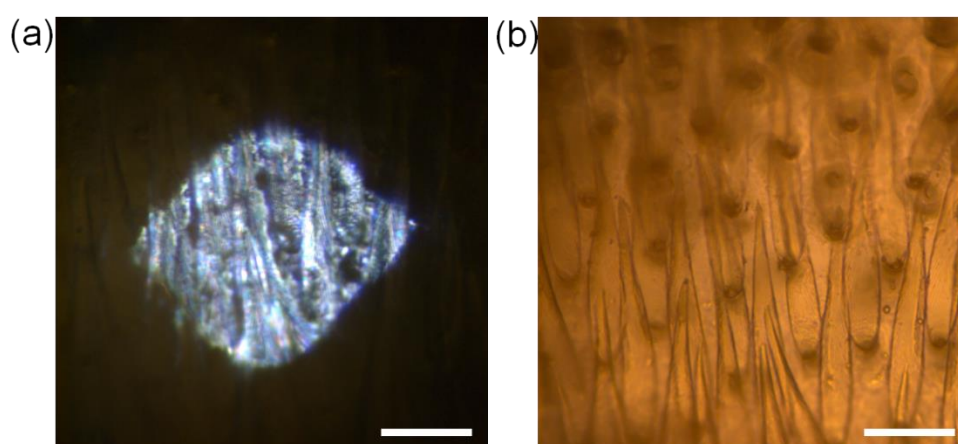
Figure S3. Bleached beetle elytra under the optical microscope. (a) Reflection mode, (b) transmission mode. Scale bare=50 μm.
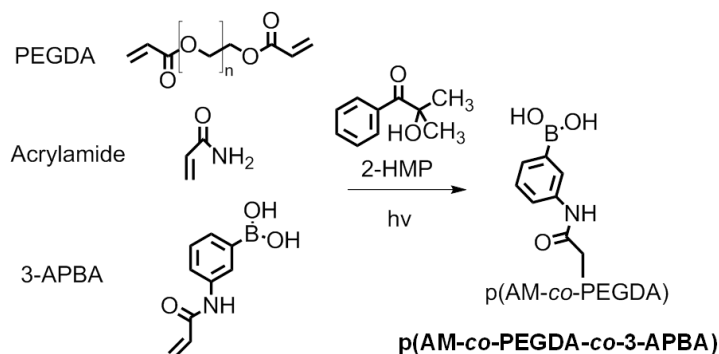
Scheme S1. Formation of p(AM-*co*-PEGDA-*co*-3-APBA) hydrogel.
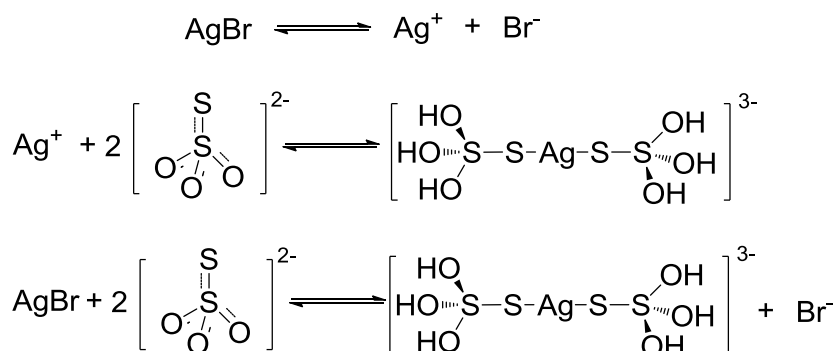
$$N = e^{\frac{-E_0}{2kT}} \tag{S1}$$

where N is the fraction of interstitial Ag^+ ion number, E_0 shows the capability of Ag^+ ions moving from the AgBr grain to the "interlattice" position, k is the Boltzman constant and T is the temperature of the NC.
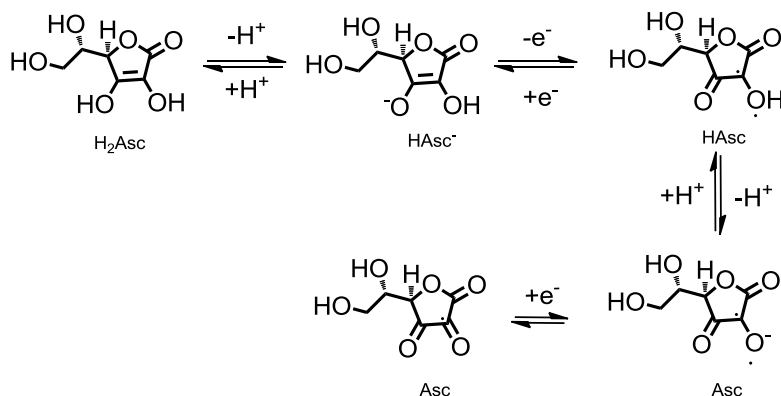
Scheme S2. Scheme incorporating sodium L-ascorbate buffer.
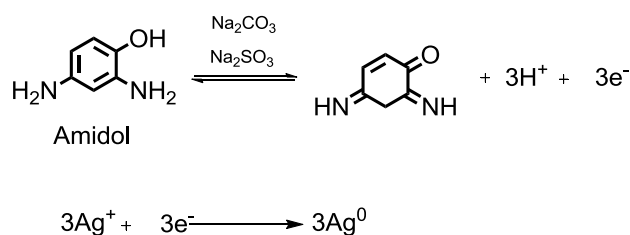
Scheme S3. Scheme showing neutral developer and Ag^+ ions.

Scheme S4. Scheme showing hypo solution and excess AgBr.

$$Ag^0 + CuSO_4 + 2LiBr \xrightarrow{\text{Acetic acid}} AgBr + Li_2SO_4 + CuBr$$

$$Cu^+ + e^- \longrightarrow Cu^0$$
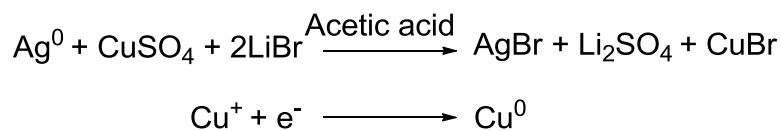
Scheme S5. Scheme showing bleaching solution.

$$HSO_4^- \longrightarrow SO_4^{2-} + H^+$$

$$Cu^0 + S_2O_8^{2-} \xrightarrow{H^+} 2SO_4^{2-} + Cu^+$$
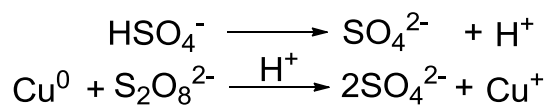
Scheme S6. Scheme showing anti-printout solution.
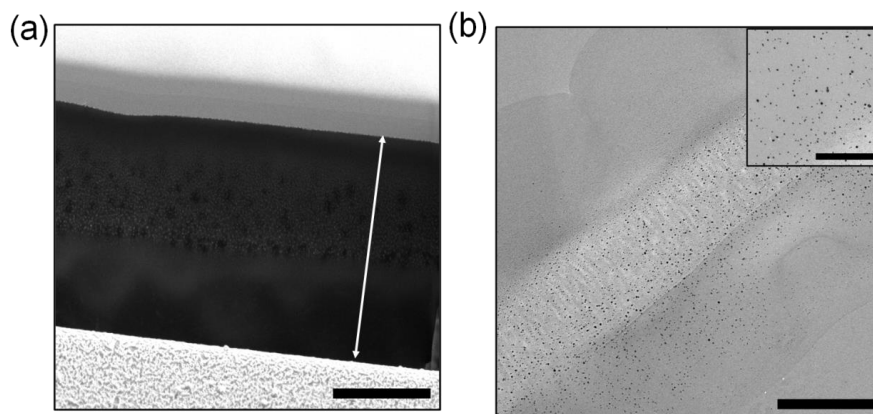
Figure S4. Morphology characterization of hydrogel film-based Bragg stacks. (a) Cross-section SEM image of hydroge film. Arrow shows the thickness of the hydrogel film. Scale bar=5 μm. (b) Ultrathin cross-section TEM image of Bragg stacks. Scale bar= 5 μm. Inset shows magnified TEM image of monodispersed Ag^0 NPs. Scale bar=2 μm.
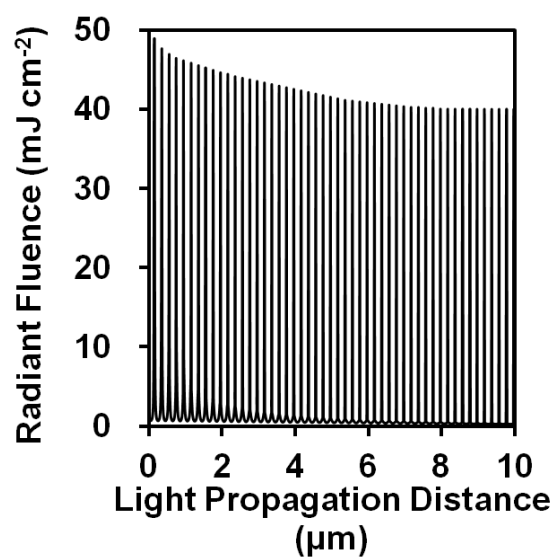
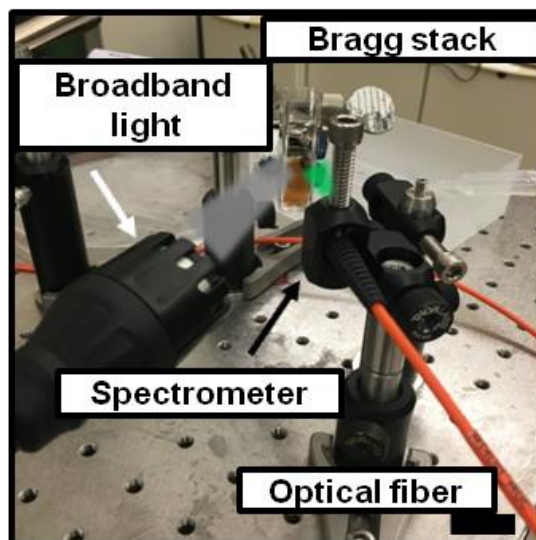**Figure S5.** Laser interference propagation within the polymer matrix. Peaks represent standing wave (antinodes).

Figure S6. The optical setup for probing the Bragg stacks and obtaining spectral measurements. Scale bar=3 cm.

(a)

(b)
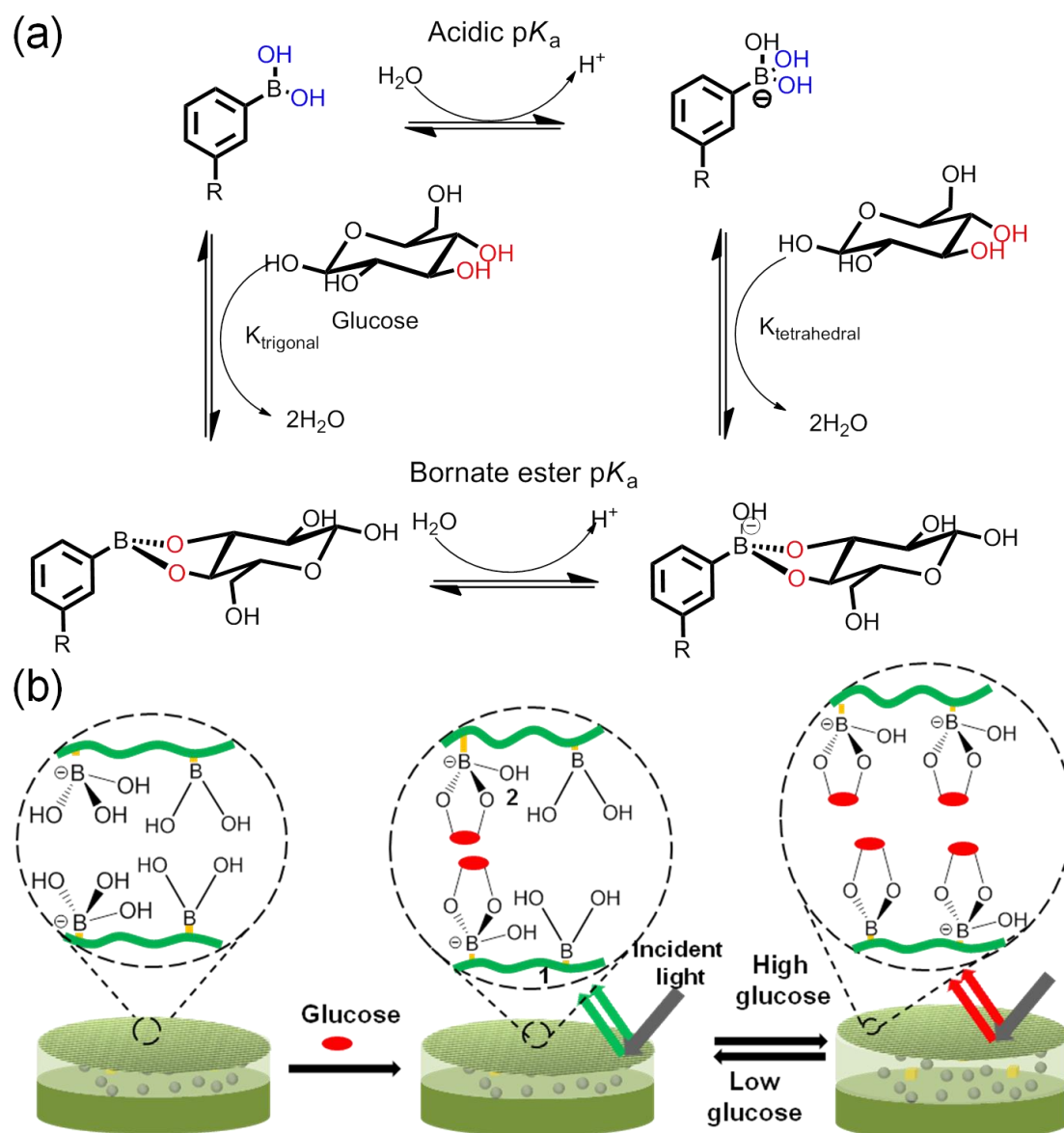
Figure S7. Principle of operation of the glucose-responsive hydrogel. (a) Complexation of the boronic acid forms with *cis*-diols of glucose molecules. (b) Reversible swelling of the hydrogel by varying glucose concentrations. (1) p(AM-*co*-PEGDA-*co*-3-APBA) backbone, (2) Complexation of anionic boronate and glucose molecules within the hydrogel matrix.

The hydrogel swelling response to glucose molecules could be modeled by Flory-Huggins theory, where hydrogel volume was affected by total osmotic pressure of hydrogel (Π_T).[32, 41] At equilibrium condition, the total osmotic pressure should be zero, which can be expressed as (Equation S2):

$$\Pi_T = \Pi_M + \Pi_E + \Pi_i = 0 \tag{S2}$$

where Π_M is the Donnan osmotic pressure related to free energy of mixing hydrogel and solvent (Equation S3); Π_E is Donnan osmotic pressure related to counterbalancing free energy of network elasticity (Equation S4); Π_i is Donnan osmotic pressure due to the difference between ion concentration inside and outside hydrogels (Equation S5).

$$\Pi_M = -\frac{\partial \Delta G_M}{\partial V} = -\frac{RT}{V_s}\left[\ln\left(1 - \frac{V_0}{V}\right) + \frac{V_0}{V} + \chi\left(\frac{V_0}{V}\right)^2\right] \tag{S3}$$

$$\Pi_E = -\frac{\partial \Delta G_E}{\partial V} = -\frac{RT n_{cr}}{V_m}\left[\left(\frac{V_m}{V}\right)^{1/3} - \frac{1}{2}\frac{V_m}{V}\right] \tag{S4}$$

$$\Pi_i = RT(c_+ + c_- - c_+^* - c_-^*) \tag{S5}$$

where R is the gas constant, T is the absolute temperature, χ is a free energy parameter associated with interaction between hydrogel network and the solvent, V_s is molar volume of solution, n_{cr} is the effective number of the cross-linked chain in the hydrogel network. V_m is the volume of relaxed hydrogel. V_0 is the volume of dry hydrogel network. V is the volume of existing hydrogel. c_+ and c_- represent concentrations of cation and anion in the hydrogel network, while c_+^* and c_-^* are concentration of cation and anion outside the hydrogel. In physiological condition, ion contribution (Π_i) can be neglected due to the high ionic strength in the solution.[32] Therefore, hydrogel volume changes (swelling and shrinkage) are attributed to the binding and breakage of glucose and boronic acid. Generally, within the hydrogel matrix, the total number of cross-linked chain (n_{cr}) contains effective numbers of cross-linked chains during hydrogel formation (n_{cr}^0) and glucose molecule binding with boronic acid groups (n_{BG}). The cross-link of hydrogel network during the p(AM-*co*-PEGDA-*co*-3-APBA) hydrogel polymerization enables the chains in their most probable configurations at the original hydrogel volume. However, the cross-linking of glucose and boronic acid allows the changes in hydrogel volume by varying glucose concentration. Since the glucose-boronic acid binding is reversible, the hydrogel can swell and shrink to the most probable configuration.

When all the glucose is released from the cross-link, the hydrogel can shift to its original volume. Thus, Π_E can be expressed as (Equation S6):

$$\Pi_E = -\frac{\partial \Delta G_E}{\partial V} = -\frac{RT n_{cr}^0}{V_m}\left[\left(\frac{V_m}{V}\right)^{1/3} - \frac{1}{2}\frac{V_m}{V}\right] - RT\frac{n_{BG}}{V} \tag{S6}$$

To keep the n_{cr}^0 constant, the hydrogel was fully swollen in buffer solution; therefore the hydrogel swelling and shrinkage at existing glucose concentrations can be determined by the concentration of glucose-boronic acid binding, which can explain the binding mechanism in Figure S8.
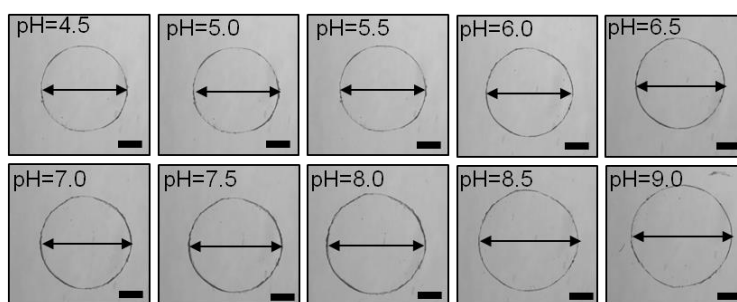
Figure S8. pH effect of hydrogel expansion. Photographs show hydrogel flake expansion with pH value increasing from 4.5 to 9.0. Scale bar=0.5 mm.

Table S3. Hydrogel flake expansion with variations of pH value.

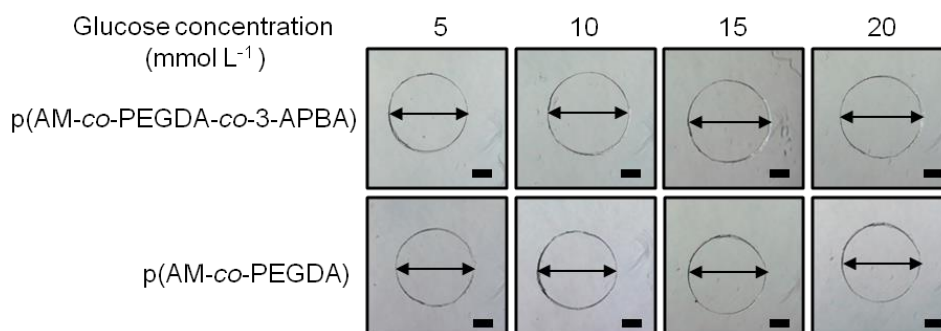| pH value	Diameter (μm)	Diameter Expansion (%)
4.5	1769	0.0
5.0	1771	0.1
5.5	1778	0.5
6.0	1789	1.2
6.5	1833	3.6
7.0	1876	6.0
7.5	1921	8.6
8.0	2008	13.5
8.5	2075	17.3
9.0	2075	17.3

Figure S9. Hydrogel flake expansion as the variations of glucose conconcentrations. Photographs show hydrogel flake expansion with the glucose concentrations increasing from 5 to 20 mmol L^{-1}. Scale bar=0.5 mm.

Table S4. Hydrogel flake expansion with variations of glucose concentrations.

Glucose Concentration (mmol L^{-1})		5	10	15	20
Diameter (μm)/ Diameter Expansion (%)	P(AM-*co*-PEGDA-*co*-3-APBA)	1939/1.4	1966/2.9	2006/5.0	2057/7.7
	P(AM-*co*-PEGDA)	1912/0.1	1912/0.1	1916/0.2	1918/0.4
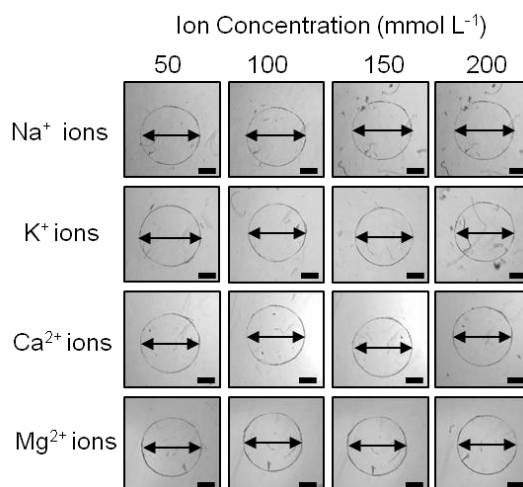
Figure S10. Ionic strength effect of hydrogel shrinkage. Photographs show hydrogel flake shrinkage with the ion concentrations increasing from 50 to 200 mmol L^{-1}. Scale bar=0.5 mm.

Table S5. Hydrogel flake shrinkage with the variation of ion concentrations.

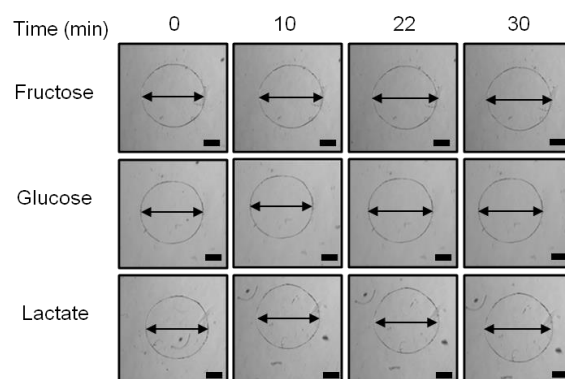| Ion concentration (mmol L^{-1})		50	100	150	200
Diameter (μm) /Diameter Shrinkage (%)	Na$^+$	1900/0.6	1896/0.7	1892/1.0	1885/1.4
	K$^+$	1896/0.8	1894/0.9	1887/1.2	1881/1.6
	Ca^{2+}	1908/0.2	1903/0.4	1898/0.7	1890/1.1
	Mg^{2+}	1906/0.3	1893/0.9	1885/1.3	1880/1.6

Figure S11. Hydrogel flake expansion in fructose, glucose and lactate solutions. Photographs show hydrogel flake expansions with the prolonged time in fructose, glucose and lactate solutions at the concentration of 10 mmol L^{-1} respectively. Scale bar=0.5 mm.

Table S6. Hydrogel flake expansion in fructose, glucose and lactate solutions with the prolonged time.

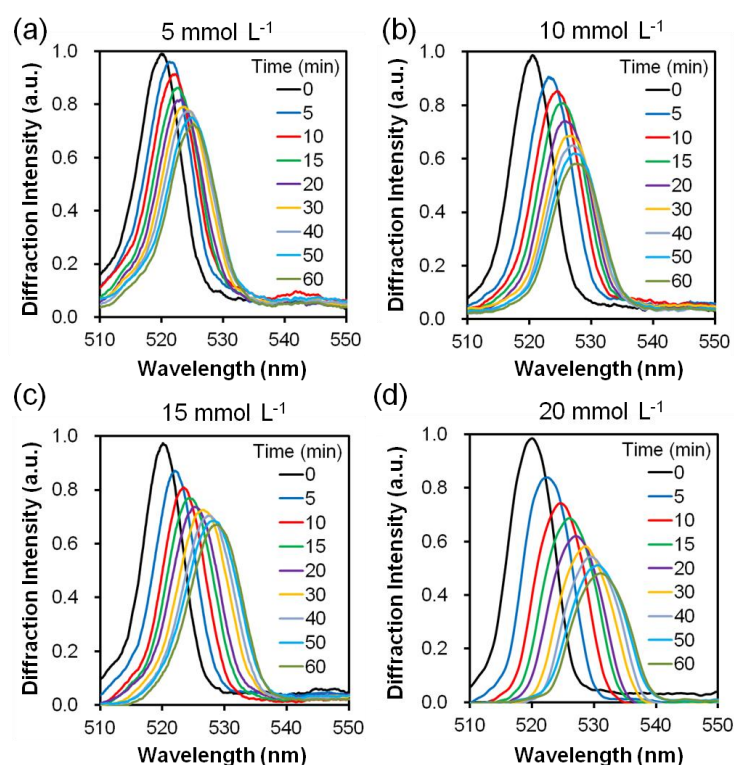| Time (min)		0	10	22	30
Diameter (μm) /Diameter Shrinkage (%)	Fructose	1911/0	1949/0.7	1964/2.8	1970/3.1
	Glucose	1911/0	1937/0.9	1955/2.3	1966/2.9
	Lactate	1911/0	1969/0.4	1971/3.2	1973/3.3

Figure S12. Response of Bragg stacks to glucose within physiological glucose range. Visible-near-infrared diffraction spectra of a photonic crystal swollen by prolonged responding time at the constant glucose concentrations. (a) 5, (b) 10, (c) 15, and (d) 20 mmol L^{-1}.
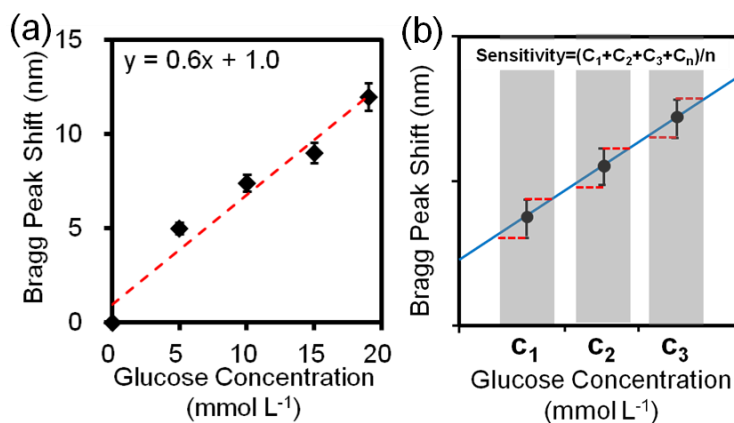
Figure S13. Calculation of sensitivity of Bragg stacks. (a) Bragg peak shifts over 1 h as glucose concentrations was varied up to 20 mmol L^{-1}, (b) Calculation of sensitivity (n=3).
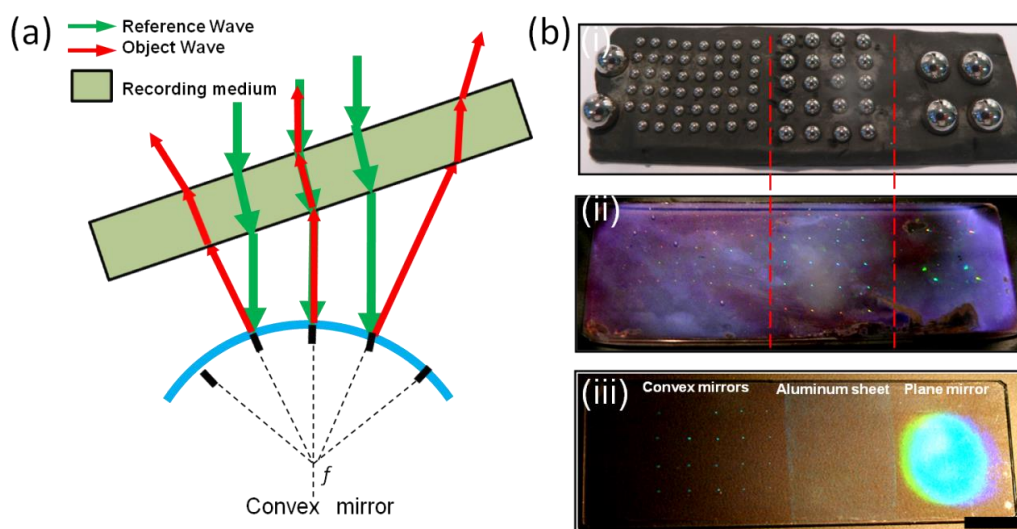

Figure S14. Bragg stacks exposed under convex mirrors. (a) A ray diagram of Bragg stacks formed using a convex mirror. (b) Photographs of Bragg stacks rocerded with convex mirrors with different diameter; (i) convex mirror with diameters of 6.0 mm, 3.0 mm, and 2.0 mm. (ii) Bragg stacks after exposure with convex mirrors; (iii) Bragg stacks exposed with convex mirrors (Ø=3.0 mm), aluminum sheet (rough surface) and a plane mirror. Scale bar=1 cm.